



PHY3004W

Grappling with Granular Gallimaufries

Thavish CHETTY, Realeboga DIKOLE, Ursula HARDIE, Erin JARVIE, Michael KONING,
Denislav MARINOV, Ntshembho MTSETWENE, Tamzyn PAYNE, Vineshree PILLAY, Robert
VAN DER MERWE, Sarel VAN DEVENTER, Kaedon WILLIAMS and Jess WORSLEY

supervised by
Dr. Tom W LEADBEATER

Department of Physics, University of Cape Town

Abstract

Through the use of UCT PEPT (Positron Emission Particle Tracking) various particle trajectory analysis methods are performed 10mm and 5mm glass beads within a tumbling mill. Various mass ratios and speeds were analysed in order to link the differing speeds and ratios to the 5mm and 10mm particle segregation.

Preface

Though classical mechanical systems are generally well understood, there are inconsistencies in the theory of granular dynamics. This creates a glitch in scientific unification, which is certainly not the case in most mechanical processes. This may be a shock to the scientifically astute. Newton's Laws permeate education from secondary school onwards, only to be fleshed out with Lagrangian mechanics in undergraduate physics classes. How can we still not perfectly predict classical systems?

The problem is generally due to an inability to model large, multi-particle, interacting systems that cannot be observed through invasive analysis. Much like the juxtaposed world of quantum mechanics, the 'physical' observation of a particle within a granular system is not a valid representation of what it is doing, did and will do. Computationally, modelling particles with so many degrees of freedom requires large simplifications to make any progress. It is well known that large multi-particle systems often have no analytical solution and require extensive computing power to model.

However, a method, that does in fact reveal the precise three dimensional trajectory of a particle in a dynamic system, does exist. This method, known as Positron Emission Particle Tracking (PEPT), can be utilized only in two places: The University of Cape Town and the University of Birmingham.

As final year undergraduates we intend to explore and add scientific value to this realm of physics. This is, of course, with the help of one of the few pioneers in this field: Dr. Tom W Leadbeater.

Contents

1	Introduction	4
2	Theory	5
2.1	Processes of interest	5
2.1.1	The Tumbling Mill	5
2.1.2	Particle Movement and Layer Formation	5
2.2	Theoretical expectations and analysis methods	8
2.2.1	Radial particle motions: Theoretical models and predictions	8
2.2.2	Axial particle motions: Theoretical models and predictions	10
2.3	Occupancy	10
2.4	Computational Work	11
2.5	Theoretical motivation for fixed variables	12
2.5.1	Constant Masses	12
2.5.2	Glass Beads	12
3	Method	13
3.1	Equipment	13
3.1.1	The Siemens HR++ PET scanner	13
3.1.2	Shape and Volume of Beads	14
3.1.3	Radionuclides for tracking and calibration	14
3.2	Geometries and setup	15
3.3	Experimental Procedures	18
3.3.1	Tracer creation and theory	18
3.3.2	Activities of the tracers	19
3.3.3	Radiation Safety	20
3.4	Calibration Measurements and optimization methods	21
3.4.1	^{22}Na Boundary Plotting	21
3.4.2	Velocity calibrations	21
3.5	Uncertainty Budget and Analysis	22
4	Data Collection and Processing	23
4.1	Raw Data Collection	23
4.2	f_{opt} method for filtering spurious LORs	23
4.3	Velocity Calculations	25
5	Analysis	26
5.1	Froude numbers	26
5.2	Radial effects	26
5.2.1	Frequency Plots	26
5.2.2	The effect of rotational speed and particle size on the S-shaped profile	28
5.3	Particle velocity plots	30
5.4	Position Probabilities	33

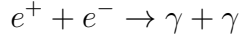
5.5	Axial Effects	36
5.5.1	Energy Fluctuations with Occupancy	36
6	Discussion and Conclusions	40
6.1	Further Work	40
6.1.1	Mayavi Python Vector analysis	41
	References	42
	A Uncertainty Budget	44

1 Introduction

Approximately 10% of the world's industry power is dedicated to handling granular materials, yet the processes are, on average, only 50% efficient [1]. Continued research into granular systems is crucial if we wish to minimise energy use in industrial processes. However there is no unified theory of granular dynamics [2].

Using the state-of-the-art technique called Positron Emission Particle Tracking (PEPT), such systems can be non-invasively observed, through measurement of coincidence annihilation gamma rays emitted by a particle containing a radionuclide which undergoes β^+ decay. The trajectory of a single particle within a system undergoing granular or liquid flow, is recorded through the triangulation of the back-to-back 511 keV positron-electron annihilation gamma rays associated with β^+ decay. This technique, which can be performed in three dimensions only in Cape Town and Birmingham, is far more accurate and revealing than any modern computer models.

The 511 keV gamma rays are emitted $180.0 \pm 0.5^\circ$ from one another due to the conservation of momentum of the electron-positron collisions[3]. The equation below details this phenomenon.



In this report we investigate the granular segregation of two different sized macroscopic particles that have the same density, material and outer texture. The axial and radial segregation is explored for particles of 10mm and 5mm diameter at varying speeds and mass ratios.

A detailed explanation of terminology associated with tumbling granular systems is presented. This report focuses predominantly on radial and axial segregation of particles and the analyses of frequency, occupancy and profile shape change as well as fluctuation energy, which can help to explain the largely unknown axial segregation of different sized particles within a flow regime of a tumbling mill.

2 Theory

2.1 Processes of interest

2.1.1 The Tumbling Mill

Our investigation is focused on granular flow within a smooth cylindrical drum with no lifter bars. This closely resembles a tumbling mill, used prolifically in industrial processes [4] and defines our fixed system for particle interaction. An example of a basic tumbling system is a half-full drum of length L . The level of the material then sits at the diameter D of the cylinder and has exposed surface area LD . Assuming that the flowing system has the same density as the fixed system and rotational speed ω , in a 180° revolution of duration $\frac{\pi}{\omega}$, all material passes the point on the cylinder intersected by the horizontal fill line. The volumetric flow rate midway through the material layer ($x = 0$ in Figure 1c) can then be calculated [5] with

$$\frac{d\Omega}{dt} = \frac{\omega L^2}{2} \quad (1)$$

Where t is time, ω is angular speed in radians per second and Ω is the solid angle.

The material in the drum may undergo both axial (along the length of the cylinder) and radial segregation. In the latter, provided a porous enough system, smaller particles will move to the bottom of the free-flowing layer and form a central core in the bulk, as seen in the mid blue region in Figure 2. Given that we are using beads rather than, for examples, grains of sand, our system will be porous enough for this to occur.

The axial process is less understood, with no unanimous theory on the mechanism behind it, other than that friction and buoyancy play a part [1].

2.1.2 Particle Movement and Layer Formation

The motion behaviour of granular material in rotating cylinders can be characterised by what is called a Bed Behaviour diagram (BBD) which shows the friction coefficient and the Froude number (see Section 2.2.1.1 for details) against the filling degree [6]. There are three major types of transverse bed motion that have been observed experimentally: slipping, cascading and cataracting. These can be further classified into sub-types, found in Table 1, each with characteristic Froude numbers.

Type	Slipping		Cascading			Cataracting	
Subtype	Sliding	Surging	Slumping	Rolling	Cascading	Cataracting	Centrifuging
Froude number	$0 - 10^{-4}$		$10^{-5} - 10^{-3}$	$10^{-4} - 10^{-2}$	$10^{-3} - 10^{-1}$	$0.1 - 1$	≥ 1

Table 1: Table showing types of transverse bed motion with their sub-types and respective Froude number ranges, adapted from Mellmann, 2001 [6].

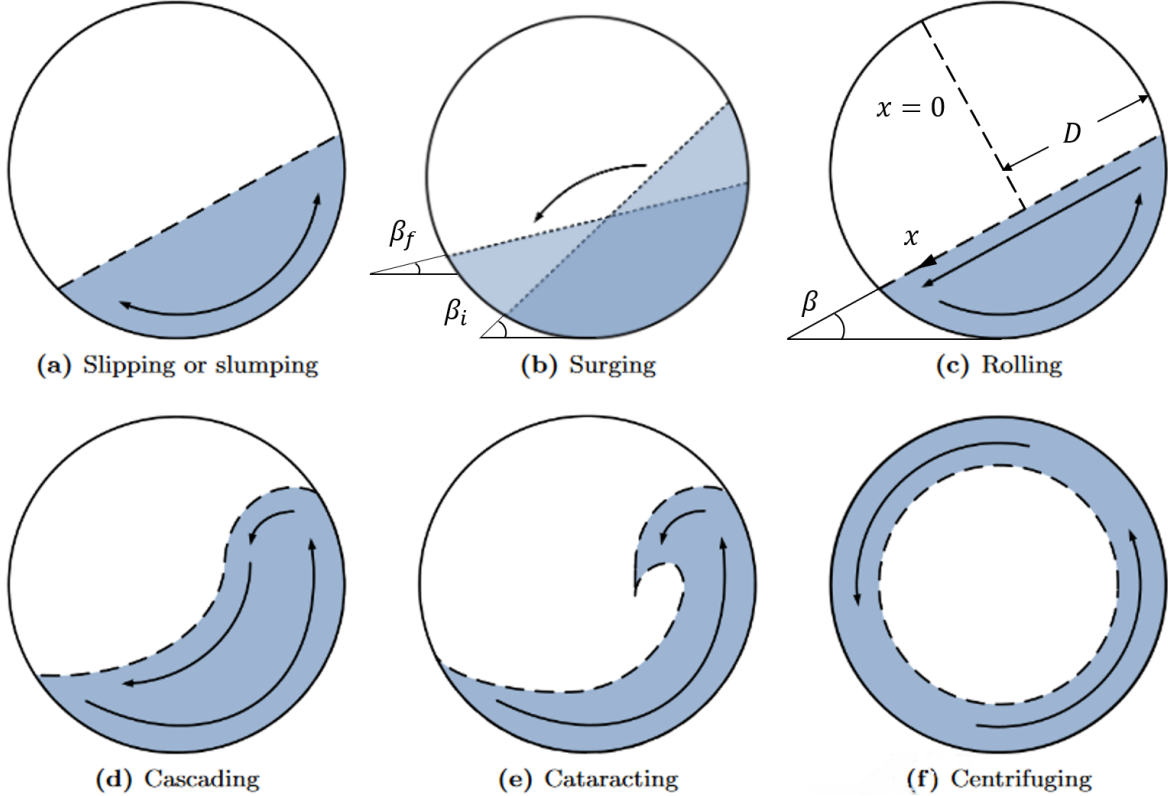


Figure 1: Diagram of flow regimes in a rotating drum with ω increasing from top left to bottom right, taken from Morrison [4] with edits from Ottino and Khakhar [5]. In the surging motion scheme, β_i and β_f are the free surface angles before and after an avalanche, respectively. Angle β in the rolling regime is the equilibrium angle of repose, which is the angle between the top of the free-flowing layer and the bottom of the drum.

During motion, the granules in the system will form distinct layers, depending on the angular speed. The very bottom layer, or rising region, follows the rotation of the drum and is generally the most dense. The active layer above it flows as a viscous liquid and is mainly driven by gravity. Its upper bound resembles an S-shaped curve, called the bulk free surface. If the system is undergoing cataracting motion, there will be an additional "free-flight" layer of granules launching from the shoulder in a dilute stream [7]. The equilibrium surface forms the boundary between the rising and active layers.

The bulk free surface is the upper bound of the bulk, while the charge free surface is the upper bound of the free-flight region. These layers can be clearly seen in Figure 2, and are divided into the shoulder and toe regions. The shoulder region consists of the leading granules at the head of the bulk free surface, and is driven forward both by gravity and the weight of the beads behind it. The beads travelling in free-flight leave the bulk at the departure shoulder. The toe region consists of the rearmost granules, and free-flight particles rejoin the bulk at the re-entry toe. The head of the shoulder region indicates the maximum height reached by the free-flying beads, while the impact toe is the point at which they touch the surface of the cylinder again.

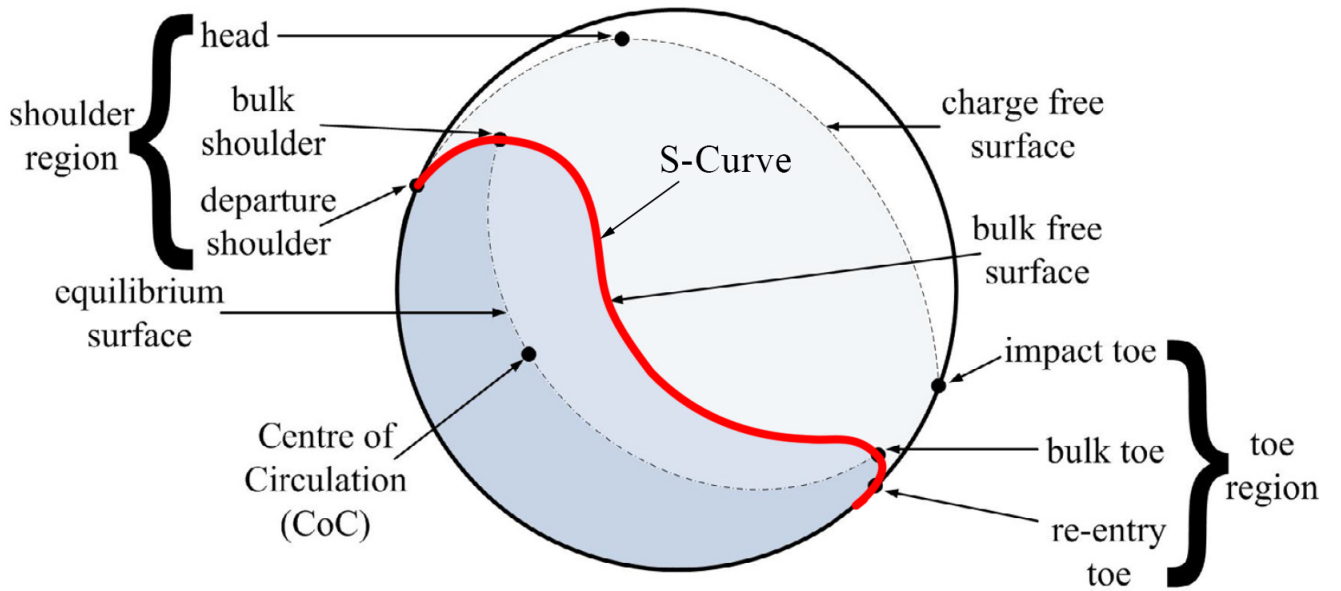


Figure 2: Labelled schematic indicating layer formation in granular media in a rotating drum, taken from Morrison, 2016 [4]. The dark blue region represents the rising layer following the rotation of the drum. The mid blue layer represents the flowing layer, bounded above by the characteristic S-curve. The light blue layer represents the free flight layer. The red line follows the path of the S-curve from the shoulder to the toe of the bulk.

2.2 Theoretical expectations and analysis methods

2.2.1 Radial particle motions: Theoretical models and predictions

2.2.1.1 The Froude number

The Froude number is the ratio of inertial (F_c) to gravitational (F_g) forces and characterises a system's flow as sub- or super-critical. It can be derived from Newton's first and second laws with

$$\begin{aligned} F_c &= m\omega^2 R \\ F_g &= mg \\ \text{Fr} &= \frac{F_c}{F_g} \end{aligned}$$

From this ratio we obtain the Froude number:

$$\text{Fr} = \frac{\omega^2 R}{g} \quad (2)$$

where ω is the angular speed in radians per second (rad s^{-1}), R is the radius of the drum and g is gravitational acceleration. A low (< 1) Froude number is a result of low rotational speed, creating a system dominated by cascading flow. A high (≥ 1) Froude number indicates a centrifugal system in which the gravitational force equals or exceeds the centripetal [8]. The critical speed, at which the layer closest to the circumference of the drum starts to centrifuge, can be calculated by setting $\text{Fr} = 1$.

$$\omega_c = \sqrt{\frac{2g}{D-d}} \quad (3)$$

where D is the drum's inner diameter and d is the diameter of each granule. When using fine granules, we can apply the condition $d \ll D$ to obtain

$$\omega_c \approx \sqrt{\frac{2g}{D}} \quad (4)$$

2.2.1.2 Modelling the S-curve

The evolution of the bulk free surface as defined in Section 2.1.2, has been studied extensively. The S-shaped profile developing with increasing speed is found to be the result of inter-particle friction (in addition to friction between the cylinder wall and the granules). The shape is often approximated using a sigmoid function of the form [4]:

$$y(x) = a + \frac{b-a}{(1+ce^{d(f-x)})^g} \quad (5)$$

A general example of this shape can be seen in Figure 3. A commonly used software is Rocky DEM which allows users to perform complex analysis on particle simulations. The sigmoid function stated above can be used along with particle simulation to determine parameters that models particular systems with varying bead size, cylinder size and rotational speed.

Different flow regimes have been identified in rotating cylinders depending on the speed of operation. Flow regimes are characterised by the Froude number given by Equation 2 in Section 2.2.1.1.

The varying bead sizes can be analyzed by using the size ratio given by the equation below.

$$s = \frac{d}{R} \quad (6)$$

Where d is the particle diameter and R is the cylinder radius. The size ratio plays a role in comparing the way granular flow varies depending on the size of spherical particles (in this case). The Froude number (F_r) and s are interrelated since both depend on the radius of the cylinder which was kept constant for this investigation. If the cylinder sizes were also varied, the usage of the s parameter would indicate the dependence of cylinder size and particle size.

Our analysis of the S-curve is to build upon the works done by A.V. Orpe and D.V. Khakhar [9] which consisted of work similar to this experiment however they used snapshot images of beads in a tumbling mill and changed the cylinder size of the mill (along with the changing rotational speeds and bead sizes). They concluded that although their methods were simple, they obtained a relationship between the flowing surface layer and S-curve profile when varying the bead size and speed. As the size ratio is decreased, the layer becomes more S-shaped. Since mixed particles were used for this investigation, the data was analyzed with respect to ratios of different sizes instead of constant bead mixtures. The dynamical angle of repose* increases uniformly with rotational speed indicating a near-linear dependence in all cases. The flow in the active layer depends primarily on the Froude number and size ratio.

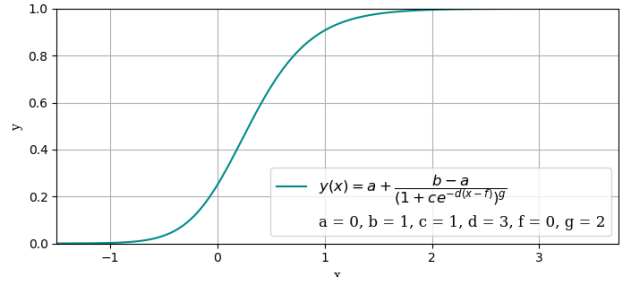


Figure 3: An example of the sigmoid function, where a and b are the upper and lower asymptotes, that relate the shoulder and toe of the S-curve, as seen in Figure 2.

*The maximum angle that a slopes of a pile of granular material can make with the horizontal before slipping.

2.2.2 Axial particle motions: Theoretical models and predictions

2.2.2.1 Fluctuation Energy

Axial segregation (along the direction perpendicular to gravity) is explained by the tendency of particles of all sizes to move away from regions of high fluctuation energy [10]. In particular, small particles are more likely to be found in regions of low energy fluctuation. This tendency is applicable to dense systems only. By observing the occupancy of the larger and smaller particles and comparing this to the fluctuation energy distribution the axial segregation can be further understood. Fluctuation energy can be found in the following way:

$$\tilde{E}_i = \frac{1}{N} \sum_{n=1}^N (\bar{v}_i - v_i^n)^2 \quad (7)$$

This is evaluated at a certain point in space over the period of time for which the cylinder rotates. \tilde{E}_i is the contribution to the energy fluctuation due to the i 'th component of velocity. \bar{v}_i is the average of all velocities (i 'th component) of particles in this region over the period of time and v_i^n is the i 'th component of the n 'th particle's velocity. N is the total number of particles that passed through this particular region of space. Once the velocity distribution is known for all points in time, \tilde{E}_i can be calculated for $i = x, y, z$, then the energy fluctuation at this point in space is $\tilde{E}_{total} = \tilde{E}_x + \tilde{E}_y + \tilde{E}_z$ [1]. If this is performed in all regions of the cylinder, an energy fluctuation distribution can be obtained and compared to the above theory.

2.3 Occupancy

An occupancy time plot [7] will show where the particle spends the least and most of it's time. An occupancy plot indicates the amount of time the particle spent at each location (Figure 4). The occupancy time at each position can be defined as half the time between the recorded time of the previous and following position data.

$$t_{occ,i} = \frac{t_{i+1} - t_{i-1}}{2} \quad (8)$$

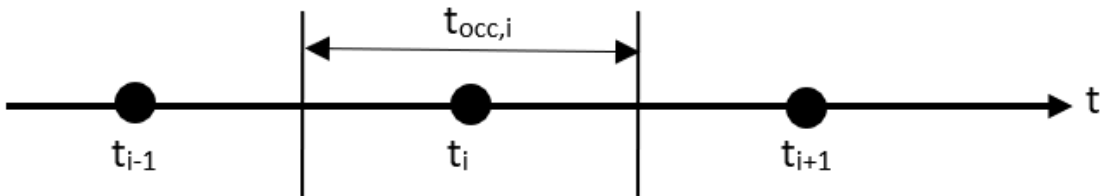


Figure 4: Diagram representing occupancy time per bin.

It is expected that the probability distribution of the 5 mm and 10 mm beads will be different due to core segregation such that distribution of one will be maximised along the boundary of the mixture while for the other, this will occur more centrally. Furthermore, the rotation speed is should influence the degree of separation, such that the area of highest probability changes for each size tracer.

2.4 Computational Work

Currently the analysis of granular systems via PEPT surpasses any computational models. This is generally due to the limited computational power and a lack of understanding of the mathematics behind granular flow [11]. The processes within the rotating drum may be simulated with models of granular particles in a fluid medium. Most models of granular flow are not derived from first principles and instead rely only on qualitative analysis. This is due to a lack of original measurements that would provide the necessary parameters for modelling [11]. Numerical models primarily used to simulate such systems are Discrete Element Method (DEM), Computational Fluid Dynamics (CFD) and Smooth Particle Hydrodynamics (SPH).

DEM traces individual particles in the system and calculates the forces between particles using Newton's Second Law[†]. This only applies to particles in direct contact. The linear (F) and rotational (Γ) forces are then calculated by summing the weights and contact forces, and moments between neighbouring particles, respectively [12].

$$F \equiv m \frac{d^2x_i}{dt^2} = \sum_{i,j=1}^N (m_i g + F_{ij}) \quad (9)$$

$$\Gamma \equiv I \frac{d\omega_i}{dt} = \sum_{i,j=1}^N (r_i \times F_{ij}) \quad (10)$$

The drawback of this method is that it does not take into account the forces propagating between non-neighbouring particles over a single time step. DEM is also limited by the available computational power, since it models individual particles, and our drum contains anywhere between 950 and 7750 granules for every run. This equates to between 10^{17} and 10^{23} contact forces.

CFD predicts the movement of particles in the system by applying conservation laws (mass, energy and momentum) to fluid dynamics. This method attempts to find numerical solutions to the Navier-Stokes equations [11] by discretizing the spatial geometry into a mesh and solving the equations over each time interval, using any of the finite difference, finite element and finite volume discretization methods [13]. Since the Navier-Stokes equations are non-linear, partial differential equations, finding the solutions requires a great number of boundary conditions and assumptions unique to the system under consideration. Besides this, the equations are also coupled, causing small errors in the motions of the particles or simplified boundary conditions to dramatically change the flow of the system.

[†] $F = ma$, if you didn't know.

SPH simulates the mechanics of continuum media, as opposed to discrete particles. It therefore does not require a mesh as the particles it models represent actual granules with mass. SPH is not applicable to the rotating drum, as a large number of particles are required in order to produce simulations with high enough resolution [14]. Even with our approximately 7000 particles, the resolution would be too low to be useful.

2.5 Theoretical motivation for fixed variables

2.5.1 Constant Masses

In this experiment, the total mass of the beads in the drum was kept constant over all runs, at 1.238 ± 0.001 kg. The purpose of this was to exclude frictional force from our variables, as it is not under study in this report. Varying the mass would vary the the total normal force and therefore the frictional force both between each bead and between the beads and the drum surface, according to $F_f = \mu_f N$, neither of which are under consideration. It should be noted, however, that the runs containing higher ratios of larger beads will be subject to greater friction due to the aforementioned equation, which we consider to be negligible.

2.5.2 Glass Beads

All the beads used were highly polished glass which meant that inter-particle friction affecting particle motion could be considered negligible. The details of these high grade glass beads are explained in Section 3.1.2. The use of glass is particularly relevant when wanting to apply this research to separation of mined minerals and other such hard granules.

3 Method

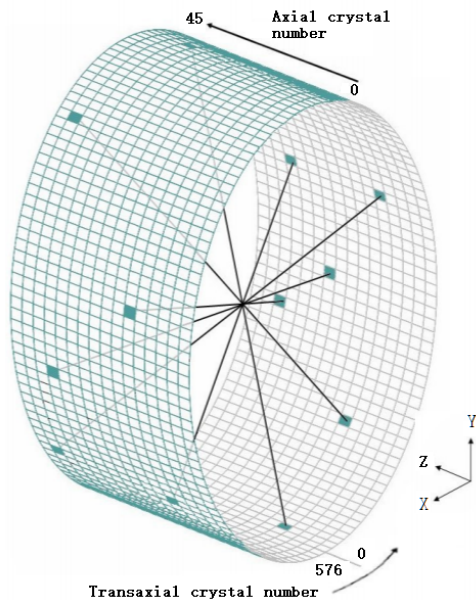
3.1 Equipment

3.1.1 The Siemens HR++ PET scanner

The PEPT imaging system used is a Siemens HR++ PET scanner[‡], shown in Figure 5a. The scanner consists of 432 bismuth germanate (BGO) block detectors arranged in a ring and has a field of view of 200mm x 600mm x 800mm [15]. Each block detector is comprised of a BGO crystal that is segmented into an 8 x 8 grid and attached to four photomultiplier tubes and associated electronics, giving the detector a total of 27648 individual detector elements. The design of these detectors allows them to be position sensitive to the grid element in which the radiation was detected.



(a) The Exact Siemens HR++ PET scanner. Located at iThemba labs, Cape Town, this machine forms part of the University of Cape Town's PEPT facility.



(b) Diagram demonstrating how multiple coincidence measurements are used to determine the position of a positron emitting isotope. Image sourced from Leadbeater, 2009 [15].

Figure 5

The detectors coincidence measurements are processed to enable tracking of the position of the tracer particle which decays via β^+ decay within its field of view. When certain proton rich nuclides decay through β^+ decay a positron and a neutrino are emitted. The emitted positron loses energy through annihilation with an electron. This annihilation releases two 511 keV gamma rays back-to-back, which are detected by the scanner in coincidence. Since the 511 keV gamma rays are emitted at $180.0 \pm 0.5^\circ$, the position of the radionuclide must be

[‡]Tactfully acquired by UCT PEPT for 1 GBP.

on the line connecting the detector elements that detected the coincidence events. This line connecting the detector elements is known as a line of response (LOR). The data processor of the PEPT detector can thereby triangulate the radionuclides position through the detection of multiple coincidence events, where the LORs intersect at the position of the radionuclide as shown in in Figure 5b.

3.1.2 Shape and Volume of Beads

The glass beads used were *Technical Beads* manufactured by PRECIOSA ORNELA. The beads are made from military grade, high purity glass and are manufactured to be almost perfectly spherical in shape with tightly controlled diameters. The beads are highly polished from thermal and chemical treatment and are resistant to extreme impact and wear. For chemical composition and material properties see [16]. These particular beads were used since their high quality and resistance to wear make them ideal for tumbling mill scenarios as they are unlikely to break or chip due to repeated impact or degrade due to exposure to radiation.

Since the segregation of mixtures of particles of different sizes is investigated, beads with diameters 5.0 ± 0.3 mm and 10.0 ± 0.5 mm were used. The volume and masses of the beads are summarised in Table 2.

Bead diameter (mm)	Volume (mm ³)	Mass (g)
5.0 ± 0.3	65.5 ± 3.9	0.16 ± 0.02
10.0 ± 0.5	523.6 ± 26.18	1.31 ± 0.02

Table 2: Volume and mass of the 5 mm and 10 mm glass beads used in the experiment.

By using beads of made of identical materials the segregation of the mixture due to particle size difference can be investigated without having to consider segregation driven by density and frictional differences.

3.1.3 Radionuclides for tracking and calibration

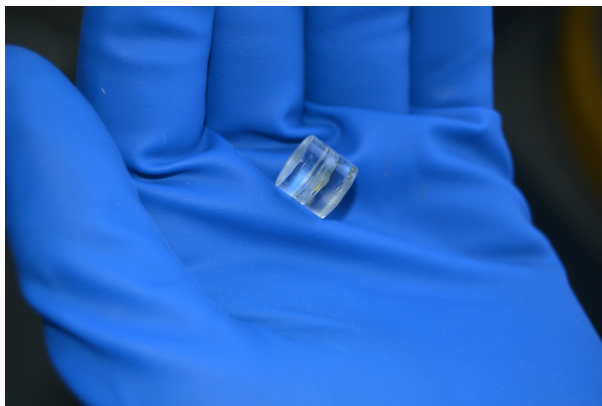
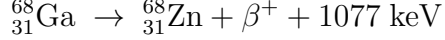


Figure 6: The ^{22}Na button source used for calibration measurements.

The PEPT detector can only track the position of positron emitting particles, so a radioactive isotope which decays through β^+ decay must be used in conjunction with the glass beads. Two different radionuclides were used in this experiment. A ^{22}Na perspex button source of approximately $17 \pm 1 \mu\text{Ci}$ was used for spacial and speed calibrations. The button source is a 10mm x 10mm cylindrical perspex button with the ^{22}Na source positioned 4mm from the bottom of the button. This source is reusable (a half-life of 2.6029 ± 0.0008 years) and was non-permanently secured to the drum.

The particle tracking was done using a tracer bead containing the radionuclide ^{68}Ga , the making of which is described in section 3.3.1. ^{68}Ga has a half-life of 67.83 ± 0.83 minutes [17]. ^{68}Ga is itself a decay product of ^{68}Ge , and decays via positron emission and electron capture to ^{68}Zn [18].



The ≈ 68 minute half life meant that in order for our data to be useful (consisting of a substantial number of LORs), measurements had to be taken within this time frame for each tracer. The specific activity of each ^{68}Ga tracer depended on laboratory condition on that day as the tracer has to be made on request. The recorded activities are detailed in Section 3.3.2.

3.2 Geometries and setup

A cylindrical metal drum with inner diameter 14.50 ± 0.05 cm and depth 7.50 ± 0.05 cm was rotated using a mechanical rig shown in Figure 7. The rig is comprised of two wheels connected to a motor powered by a DC voltage supply. Attached to the rig is a control box which can be used to control the direction and speed of rotation of the wheels. The rig is capable of rotating the wheels at speeds between 0.5 rev s^{-1} and 2.99 rev s^{-1} in a clockwise or anticlockwise direction. However, these speeds are not the drum's angular velocities (see Section 3.4.2). The drum used has clear Perspex faces that are secured with screws such that the faces can be removed and replaced at will. The 5 mm and 10 mm glass beads described in section 4.3 were placed inside or removed from the drum by removing one of the perspex faces which was then re-secured.

The rig and drum were placed on an adjustable bench running through the field of view of the PEPT detector. The height of the bench was adjusted such that the drum was in the center of the y axis of the detector, indicated in Figure 8. A spirit level was used to ensure that the bench was level.

The position of the rig was adjusted such that the drum was in the center of the field of view of the detector with respect to the x and z axes, shown in Figure 10. This positioning was done with the aid of the lasers installed on the detector which indicate the edges of the field of view. The importance of centering the drum well within the detector is to avoid large uncertainties at the fringes of the detector. A positional calibration measurement was taken to ensure that the drum was placed in the center of the field of view.

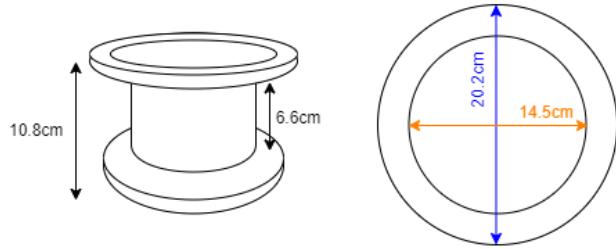


Figure 7: Diagram showing the dimensions of the rotating drum used to contain the glass beads. The beads were contained within a depth of 7.50 ± 0.05 cm and a cylindrical radius of 14.50 ± 0.05 cm.

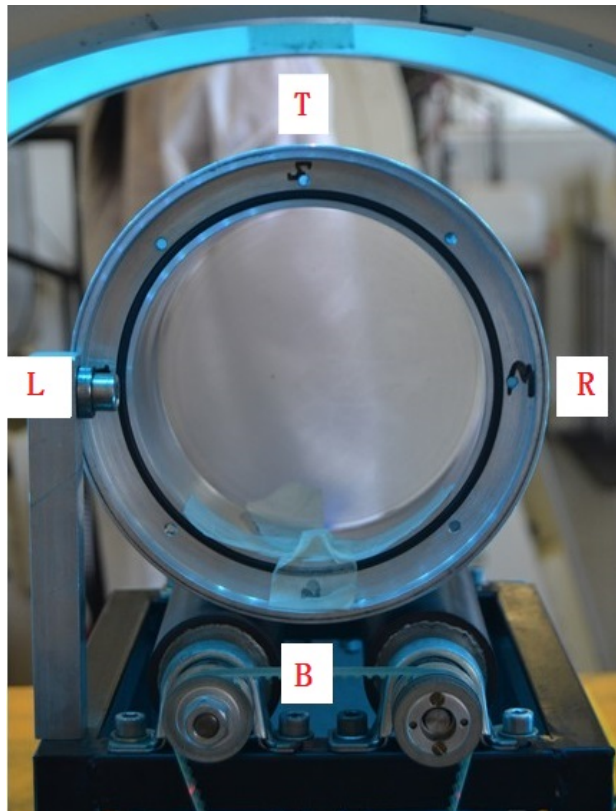


Figure 8: Image of the drum placed inside the PET scanner. The T, R, B, L labels refer to Top, Right, Bottom and Left respectively. The calibration points used followed this labelled co-ordinates system.

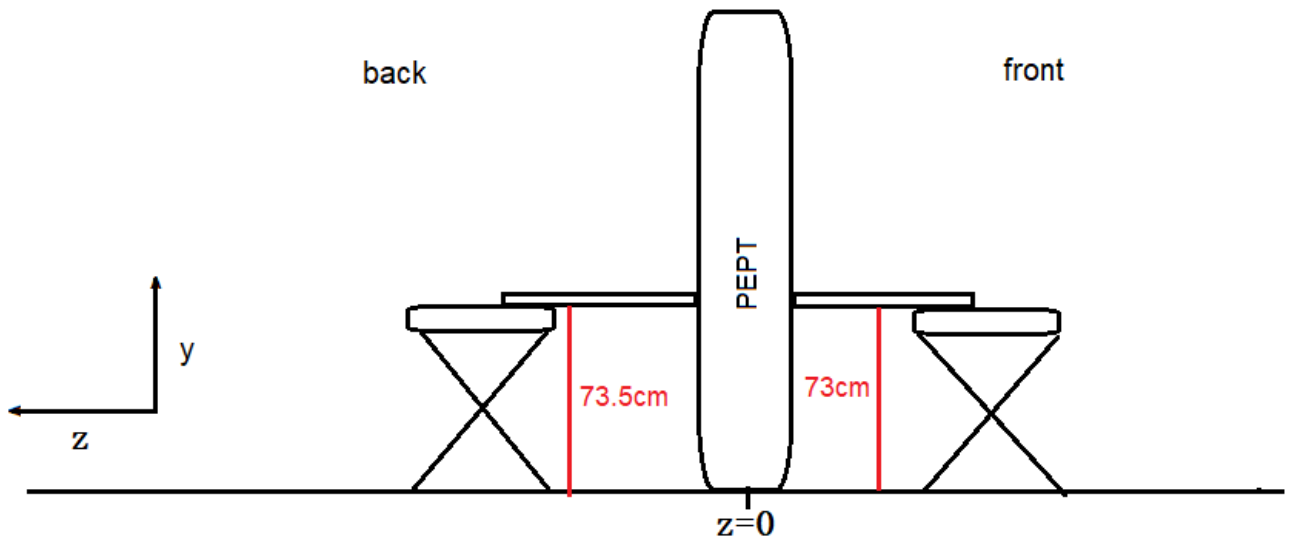


Figure 9: Diagram of the setup of the experiment showing the height of the benches and the orientation of the co-ordinate system used. In the experimental method to follow 'front' refers to positive z while 'back' refers to negative z .

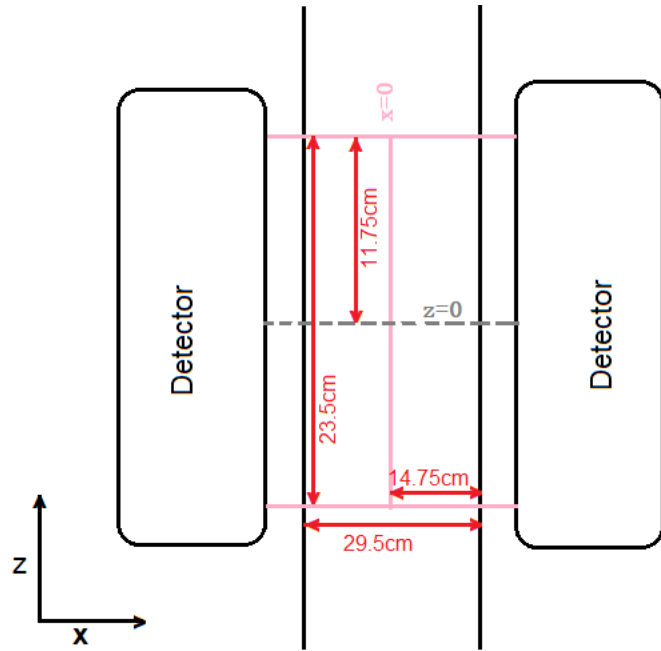


Figure 10: Diagram showing the measurements of the field of view of the detector and the orientation of the co-ordinate system. The pink lines indicate the lines drawn by the lasers installed in the detector. The rig was placed such that the center of the drum was at the center of the field of view, at $x=0$, $y=0$, $z=0$.

3.3 Experimental Procedures

The drum was filled with glass beads in the ratios shown in Table 3 and measurements with a 5 mm tracer bead were taken at low, medium and high velocities, where 'low', 'medium' and 'high' refer to the wheels of the rig rotating at 1 rev s^{-1} , 2.04 revs^{-1} and 2.99 rev s^{-1} respectively as indicated by the control box. The 5 mm tracer was used in order to track the motion of the 5 mm beads in the mixture. The measurements were taken for 10 minutes per mixture and speed setting. Between each measurement the cylinder was agitated to return the mixture to an unsegregated state. This would ensure that the tracer had to enter a new 'state' and would not get caught in the previous runs flow patterns. The same procedure was repeated with a 10 mm tracer bead in order to track the motion of the 10 mm beads in mixtures where the 10mm beads were present.

Ratio 5 mm: 10 mm	Mass 5 mm beads (kg)	Mass 10 mm beads (kg)
1:0	1.238 ± 0.001	0.000
3:1	0.929 ± 0.001	0.310 ± 0.001
2:1	0.825 ± 0.001	0.413 ± 0.001
1:1	0.619 ± 0.001	0.619 ± 0.001

Table 3: The ratios of 5 mm to 10 mm beads and the corresponding masses of each bead type. The ratios were determined via mass through the use of a digital scale.

3.3.1 Tracer creation and theory

A successful measurement on the PEPT apparatus requires that the tracer be labelled with a radionuclide of high enough activity to accurately triangulate it's location [19]. To obtain meaningful results, the tracer needs to have a suitable half-life and activity as well as suitable chemical and physical stability. This makes the technique used to create the radioactive tracer fundamental to our measurements[20].

A $^{68}\text{Ge}/^{68}\text{Ga}$ generator (Figure 11) that uses hydrochloric acid (HCl) as a solvent is used to elute ^{68}Ga . Elution is the process of extracting one substance, the eluent, from another using chromatography methods. The eluent is then treated with diluted hydrochloric acid. The Ga solution is then introduced to strongly acidic ion exchange resin beads [21]. The acidic cation exchange resins used are NRW 100 and AG50W-X4 made of organic polymer matrices and sulfonic acid exchange sites. They are obtained from manufacturers and have been found to be adequate for use as PEPT tracers in preliminary studies [22]. The $^{68}\text{Ge}/^{68}\text{Ga}$ generator, which functions as a column in chromatography, is loaded with ^{68}Ge , and elutes the daughter radionuclide ^{68}Ga . 4.5 ml of 0.6 M HCl is used to obtain the eluent ^{68}Ga in HCl. The eluted solution is decanted into a 200 ml Teflon beaker and preheated to 250°C , causing the

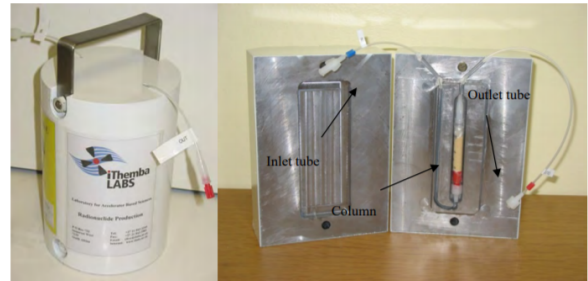


Figure 11: The $^{68}\text{Ge}/^{68}\text{Ga}$ generator used to create the tracers [21].

solution to evaporate fully in around 25-35 minutes. The solution is redissolved in 300 μL of 0.005 M HCl that serves to reduce the acidity of the ^{68}Ga solution, creating preferable radiolabelling conditions. The ^{68}Ga solution is then added to a vial that contains 2-4 strongly acidic carbon exchange beads that have a diameter of $475 \pm 10\mu\text{m}$ each, with several being added to improve reliability of the procedure. The vial is sealed and placed on an orbital shaker [22] for 30 minutes to absorb ^{68}Ga . The radionuclide is then placed inside a glass bead and sealed ready to be tracked by PEPT.

3.3.2 Activities of the tracers

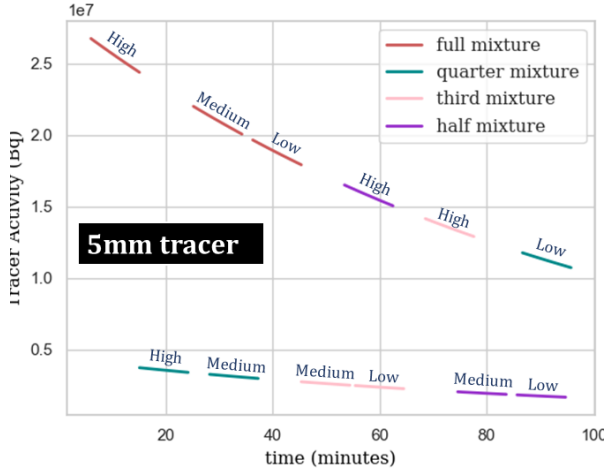
There were four different tracers used for these experiments, each with a different initial activity shown in Table 4. The change in activity over the experimental time period is calculated via:

$$A(t) = A_0 \exp \left[\frac{\ln(2)t}{T_{1/2}} \right] \quad (11)$$

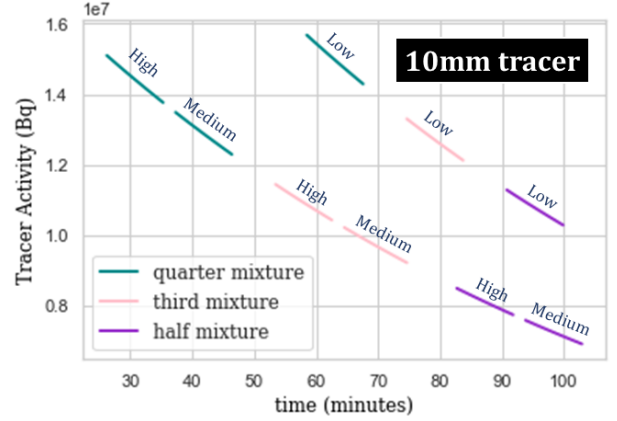
Where A_0 is the initial activity, t is time elapsed since creation, and $T_{1/2}$ is the half life of ^{68}Ga . For reference see *Radiation Detection and Measurement* (p.2 [23])

Tracer particle	Activity (10^7 Bq)	Time of creation
5mm glass bead	3.54 ± 0.01	26/09/19 at 15:09 p.m.
10mm glass bead	1.97 ± 0.01	26/09/19 at 17:19 p.m.
5 mm glass bead	2.85 ± 0.01	30/09/19 at 13:36 p.m.
10 mm glass bead	4.22 ± 0.01	30/09/19 at 14:19 p.m.

Table 4: Table showing the four ^{68}Ga tracers used in the experiment including their activity and time of creation. Two distinct tracers were used for both the 5mm and 10mm glass beads.



(a) Figure showing the decreasing activity of 5mm bead glass tracers for the different measurement conditions with the measurement condition order correlated to the decreasing activity.



(b) Figure showing the decreasing activity of 10mm bead glass tracers for the different measurement conditions with the measurement condition order correlated to the decreasing activity.

Figure 12

The approximate activity for each experimental run is detailed for both the 5mm and 10mm tracers used in Figures 12a and 12b. In these figures the terms 'high', 'medium' and 'low' refer to the 3 different drum speeds. From the figures above it can be seen that the 5mm tracer for high and medium speed quarter ratio, medium and low third ratio and medium and low half ratio measurements had a substantially lower tracer activity. This indicates that these measurements will have less LORs per unit time compared to the other measurements.

3.3.3 Radiation Safety

Those who worked directly with the PEPT scanner needed to attend some radiation training, provided by iThemba labs. Members who would be closest to the radionuclides were kitted with radiation dose monitors to account for the accumulated radiation the person will have received. Protective gear in the form of disposable lab coats, disposable shoe covers and thick gloves were worn in Blue areas (see Table 5. The red areas were strictly for radiation workers. No objects within the radiation zone were came into contact with skin. The tracer was handled exclusively by Michael van Heerden who is a certified radiation worker and works for iThemba LABS. When exiting the lab, the gloves, shoe covers and lab coats were removed. They were immediately disposed of within the confines of the radiation zone and each member was test for radiation contamination. Finally the radiation monitors were inspected for the dose every person who entered received to ensure it was below the recommended daily dosage for civilians in blue controlled areas (see Table 5). ^{68}Ga is a

Controlled Area	Dose rate
Clear Area	< 0.5 mSv/annum
Blue Area	\leq 0.2 mSv/hr
Red Area	> 0.2 mSv/hr

Table 5: Controlled area classification at iThemba labs and corresponding maximum dose limit, taken from iThemba Labs Radiation Protection Standard [24]

radioactive liquid. Though it is sealed within the tracer particle the radiation procedures detailed are mandatory for this work.

3.4 Calibration Measurements and optimization methods

3.4.1 ^{22}Na Boundary Plotting

In order to calibrate the data processing algorithm, a ^{22}Na source was secured to the drum. A reading was then taken for 30 seconds in order to identify where the data point was recorded as being. Data was taken in this manner on the top, bottom, left and right of the drum on the surface, with these readings repeated on the opposite side of the drum (see Figure 9). This data was then used to ensure that the drum was correctly positioned on the z-axis, as this simplifies the data processing and keeps the majority of the data in the central region where uncertainties are the lowest. When taking data again, these calibration readings were replaced by a single reading with the ^{22}Na source secured to the side, and the drum spinning at one revolution per second. This simplified calibration sped up the process and allowed for a quick measurement of how close to being on axis the drum was placed.

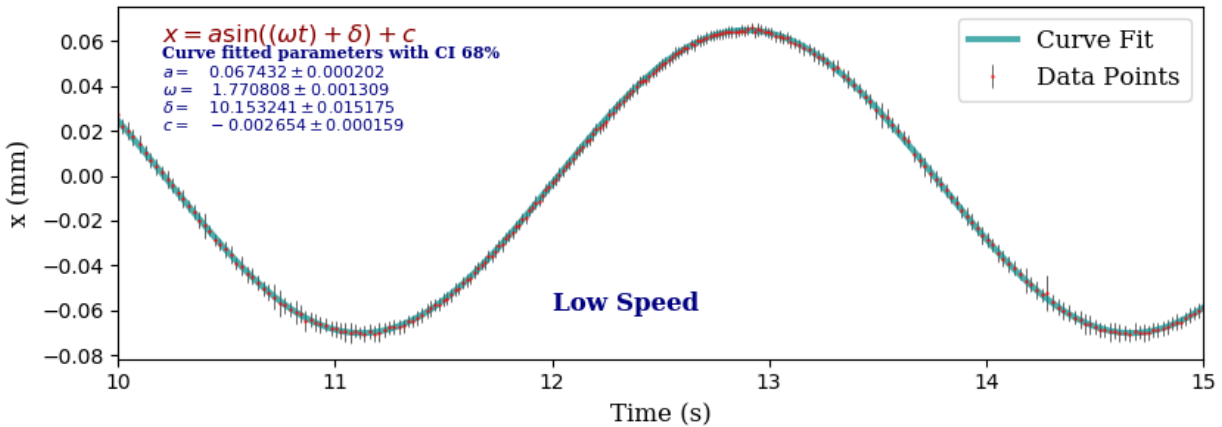
3.4.2 Velocity calibrations

The motor that set the rotation of the drum had speed settings of 1 rev s^{-1} , 2.04 rev s^{-1} and 2.99 rev s^{-1} as indicated on the control box. However, these speeds indicated the speeds at which the wheels of the rig are rotated by the motor, and thus a speed calibration must be performed in order to find the drums rotational speed. This is due to the differing radii of the drum and the rig wheels.[§]

For this calibration the drum was filled with $1.238 \pm 0.001 \text{ kg}$ of 5mm glass beads with the ^{22}Na source still secured to the inside. The drum was placed such that ^{22}Na source was at the forward-facing side, and 3-minute measurements were taken with the rig rotating at the three aforementioned velocities in an anticlockwise direction.

To find the angular speed, a sinusoidal curve was fitted to a segment of the $x(t)$ data using `scipy.optimize.curve_fit` [25], from which a value for ω with uncertainty was extracted. Figure 13 shows these sinusoidal curves for the rig rotating at varying speeds.

[§]There is also an element of mistrust associated with the meaning of the control box settings. In any case this is a crucial process in defining the speeds of drum rotation.



(a) 1 rev s^{-1} .

Figure 13: Sinusoidal fit to a 5 second region of the x-coordinate as a function of time, with curve fitting parameters displayed on the plots. Each graph represents the mechanical rig at a different speed.

To find the linear speed, the magnitude of the velocity was found as a function of time. The mean and standard deviation of these magnitudes were calculated using the `numpy` modules for each run. Table 6 shows the linear and angular speed of the drum with the rig rotating at low, medium and high speeds.

Motor speed (rev s^{-1})	Linear speed (m s^{-1})	Angular speed (s^{-1})	Froude number
1 (Low)	0.119 ± 0.004	1.7708 ± 0.0003	0.0232 ± 0.0003
2.04 (Medium)	0.242 ± 0.005	3.6169 ± 0.0003	0.0968 ± 0.0003
2.99 (High)	0.352 ± 0.006	5.3166 ± 0.0003	0.2091 ± 0.0003

Table 6: The linear and angular speeds of the drum with the motor rotating the rig at low, medium and high speeds.

3.5 Uncertainty Budget and Analysis

In this experiment our uncertainties were analysed with both a type A (based on pure statistical analysis) and a type B analysis (based on manufacturing and scientific judgement based on significant figures). The uncertainty budget (Appendix) details the type of uncertainty used

4 Data Collection and Processing

4.1 Raw Data Collection

The data is detected via the PET scanner, as described in Section 3.3, through indication coincidence measurements on detector units. The data is defined via the pair of detectors in which the coincidence occurs, which in turn defines two points in 3-dimensional space corresponding to the detector locations. Between these detectors positions, a line of response (LOR) is generated, connecting the two and defining a line on which a positron annihilation event must have occurred. Many LORs are needed to define a position with a low uncertainty per unit time. These LORs are then filtered and processed into positional data points with uncertainties providing a trajectory of the particle.

4.2 f_{opt} method for filtering spurious LORs

When collecting empirical data using PEPT, it is inherent, within data processing methods, to attain false positive and corrupted lines of response originating largely from characteristic photon scattering, detection system dead-time and random coincidences [3]. To discard these corrupted LORs and locate the tracer with minimal uncertainty, an iterative triangulation approach, known as the f_{opt} method, is applied. Initially, we take N lines of response and calculate the minimum distance point that minimises the sum of the perpendicular distances between the LORs and that point. The first minimum distance point is taken as the initial estimate of the tracer location. Thereafter, the LORs furthest from this point are considered corrupted and are removed from the next iteration of the triangulation. The process is repeated until we obtain some fraction, f , of remaining LORs from the initial set of lines as depicted in Figure 14. We obtain the optimal fraction, f_{opt} , that results in the minimum sum of the perpendicular distances which indicates the precision of the tracer location.

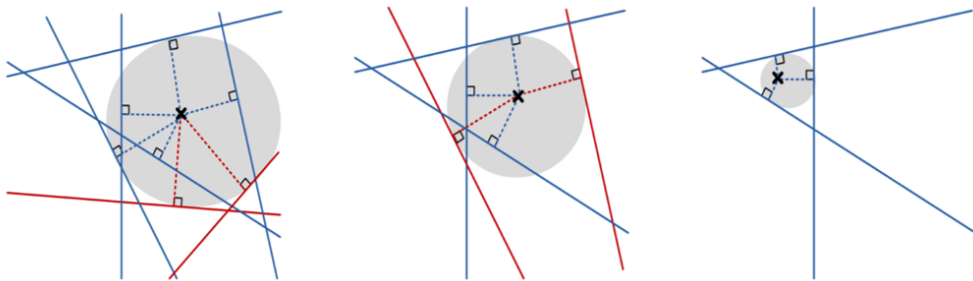


Figure 14: Depiction of the iterative triangulation process that removes corrupted LORs after each iteration.

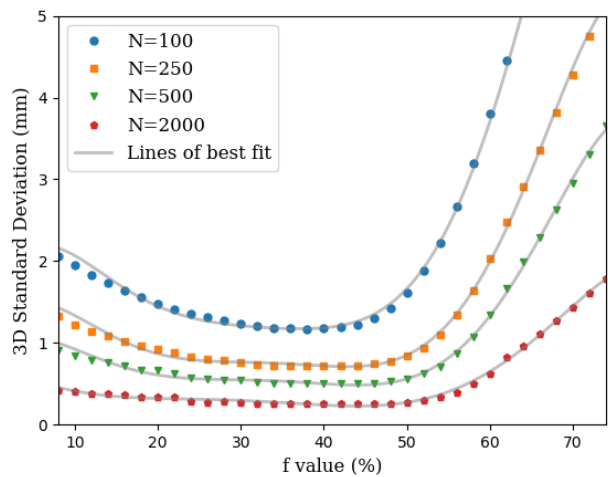


Figure 15: 3D standard deviation as a function of f produced at different values of N and fitted with 6th degree polynomials. A plateau is observed between $f = 30$ and $f = 45$ where the uncertainty associated with the tracer location is at a minimum. $f_{opt} = 40$ was chosen as an appropriate choice to obtain minimal uncertainty.

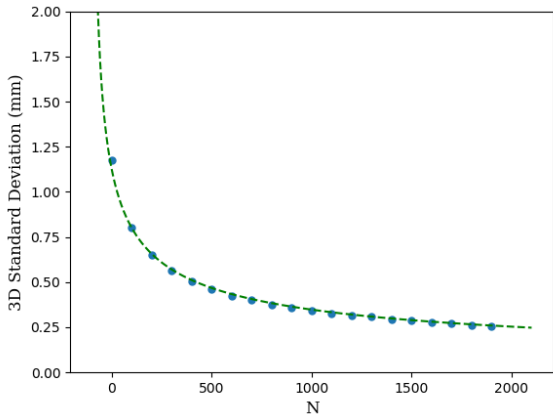


Figure 16: 3D standard deviation as a function of N with the line of best fit exhibiting an inverse square relation.

In this experiment we found f_{opt} by passing calibration data through *ctrack*, an iterative triangulation software compiled by T.W. Leadbeater that calculates the minimum sum of perpendicular distances and outputs the corresponding standard deviation. Plotting this standard deviation against the fraction f , as seen in Figure 15, offers a visual representation of how it behaves as a function of f . The graph contains curves taken with different values for N . We notice that the graphs tend to plateau between $f = 30$ and $f = 45$. It is within this region that we find the minimum 3D standard deviation and thus f_{opt} . Hence, $f_{opt}=40$ is an appropriate choice to limit the uncertainty associated with the tracer location.

The precision, Δ , of the final stationary tracer location is given by $\Delta = \frac{w}{\sqrt{fN}}$, where w is the spatial resolution of the detection system measured to be close to 5mm [3]. Referring to Figure 16, at $f_{opt} = 40$, we can observe the expected inverse square relation between the precision and N . To improve the precision of the results for a stationary tracer, one needs to use a sufficiently large N . However, for a moving tracer, each set of N events does not converge on a single point because the LORs spread across the trajectory of the moving tracer. Hence, N should be reduced to compensate for this spread. This inadvertently reduces location precision but prevents location distortion.

4.3 Velocity Calculations

Once positional data had been obtained for each run using *ctrack* with $f_{opt} = 40$, the velocities of the tracer particle could be determined. This was done using a 6-point averaging method [3]:

$$\vec{v}_i = 0.1 \left[\frac{\vec{P}_{i+5} - \vec{P}_i}{t_{i+5} - t_i} \right] + 0.15 \left[\frac{\vec{P}_{i+4} - \vec{P}_{i-1}}{t_{i+4} - t_{i-1}} \right] + 0.25 \left[\frac{\vec{P}_{i+3} - \vec{P}_{i-2}}{t_{i+3} - t_{i-2}} \right] \\ + 0.25 \left[\frac{\vec{P}_{i+2} - \vec{P}_{i-3}}{t_{i+2} - t_{i-3}} \right] + 0.15 \left[\frac{\vec{P}_{i+1} - \vec{P}_{i-4}}{t_{i+1} - t_{i-4}} \right] + 0.1 \left[\frac{\vec{P}_i - \vec{P}_{i-5}}{t_i - t_{i-5}} \right] \quad (12)$$

In this equation, \vec{v}_i is the velocity of the i th measured position, \vec{P}_i is the i th measured position, and t_i is the time at which the position was measured. For uncertainty on the velocities, a rule of thumb 10% uncertainty was applied to each coordinate of each calculated velocity vector.

5 Analysis

5.1 Froude numbers

For our cylinder of inner diameter 14.50 ± 0.01 cm we obtain a critical speed of $\omega_c \approx 11.63$ rev s $^{-1}$. Given that our focus is primarily on cascading motions, our angular speed will never exceed ω_c . We are working with rotational speeds between 1.7708 ± 0.0003 and 5.3166 ± 0.0003 s $^{-1}$, in the Froude number range of 0.0232 ± 0.0003 to 0.2092 ± 0.0003 . We will therefore expect to see rolling, cascading and cataracting motions in our drum, according to Table 1.

5.2 Radial effects

The analysis in this section specifically details particle segregation, and observed characteristics within the xy plane of our data collection. See Figure 8b for a visual indication.

5.2.1 Frequency Plots

Once positional data was obtained for each experimental run, positional frequency or 'visitation' heat maps of xy (radial) can be plotted. In Figure 17 below the x and y coordinates are binned into $1\text{ mm} \times 1\text{ mm}$ areas, with saturation indicating the number of visits in that bin.

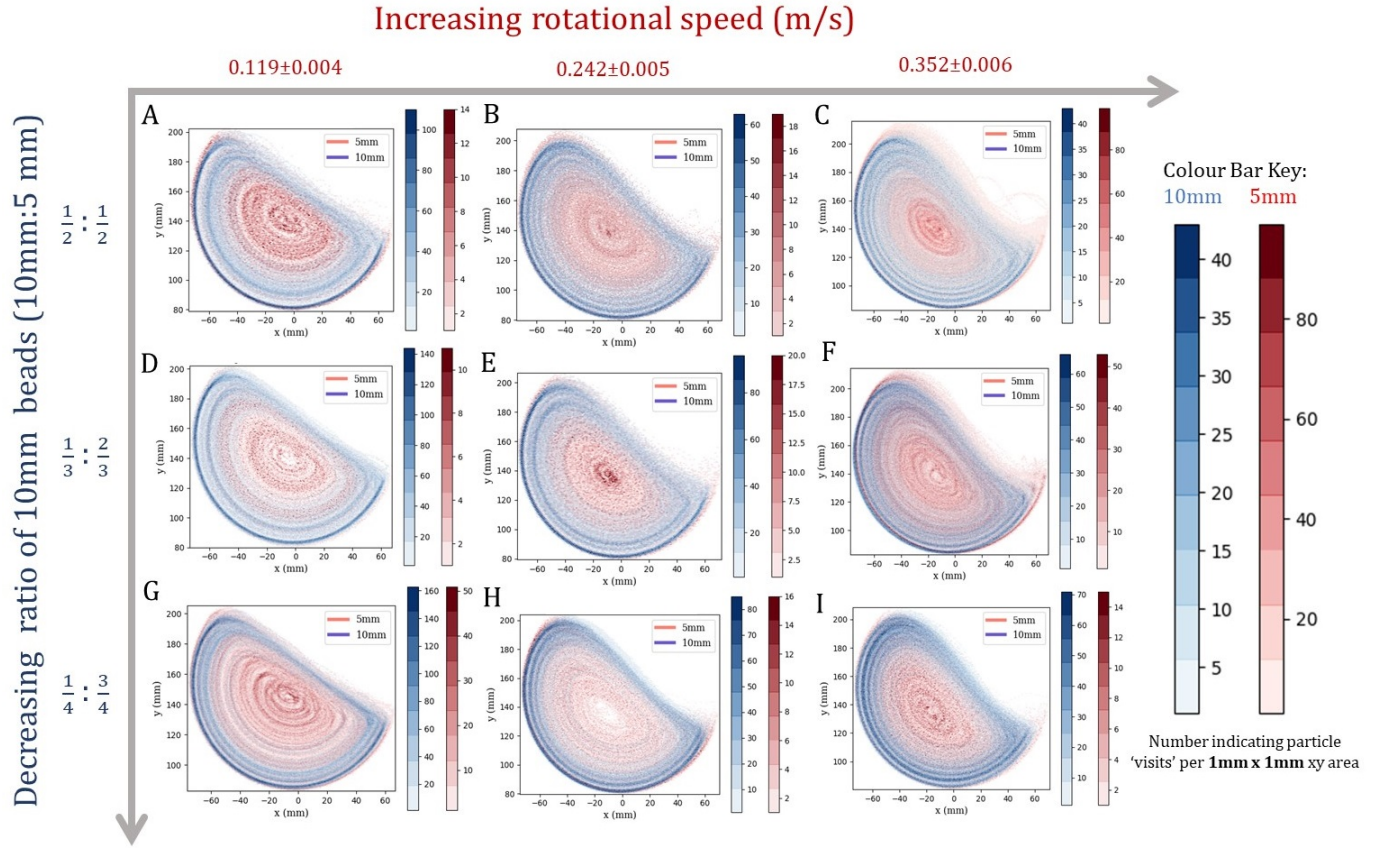


Figure 17: Binned frequency plots of radial position for the 5 mm (red) and 10 mm (blue) beads, with varying rotation speeds and bead mixtures.

In all permutations of differing speed and bead ratios, the 10 mm beads tended to remain towards the outside of the drum. Conversely, the 5 mm beads collected in the center of circulation. However as speed increases the beads exhibit more erratic visitations. The bands of circulation (red) become less profound as the motor was turned up implying that the 5 mm beads dispersed more from the center of circulation. As the ratio of 10 mm beads decreased, we see that the 10 mm beads are confined to a narrower region towards the outside of the drum. These observations are discussed in more detail in the section on Position Probabilities.

As the rotational speed of the drum increases, we can also see that the flow regimes begin to change. At the lowest speed, we can see rolling motion, with the bulk free surface being almost linear in the xy plane. As the speed is increased from this minimum, in all mixtures we can see a slow transition into cascading motion, with the bulk toes and shoulders becoming more pronounced as the rotation speed increases, and the bulk free surface attaining more of the characteristic S-shaped curve as described earlier. We can also see that the angle of the bulk free surface increases with increasing rotational speed, as expected. However, especially in the half and third ratios with the highest speed (plots C and F) the 5 mm particles (red) exhibit completely different motions to the 10 mm. The 5 mm particles run over the 10 mm particles on the bulk free surface and even enter free flight motions before hitting the impact toe of the drum and re-entering the flow regime.

The centre of circulation, indicated by the tight red oval shapes in the centre of all diagrams, move slightly towards the left (less than 5 mm) as the rotation speed increases. This behaviour is not affected by the differing ratios of particles.

5.2.2 The effect of rotational speed and particle size on the S-shaped profile

The plots in Figure 18 show the flowing bulk surface layer of granules in the rotating drum for various mixtures of bead sizes. The different flows can be divided into a flowing surface layer and a fixed bed rotating at the angular velocity of the cylinder. The data extracted in Figures 18 and 19 is the profile extracted from the surface layer of the flow.

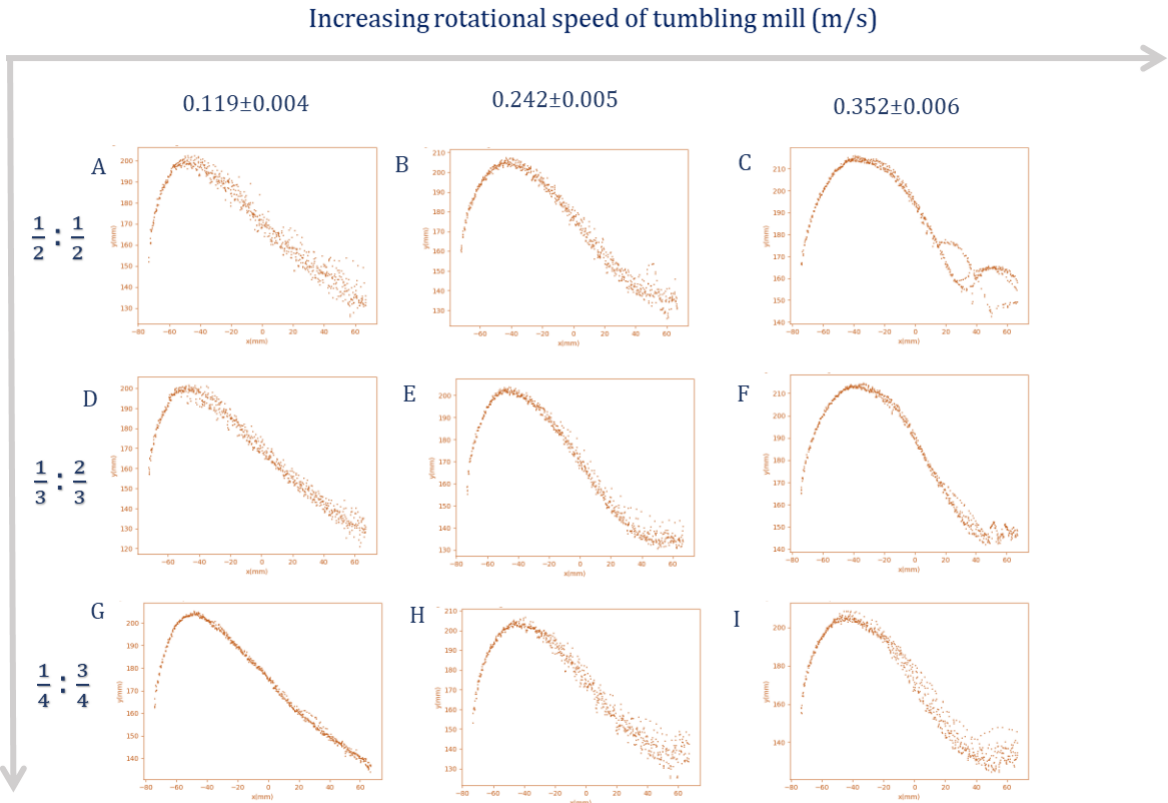


Figure 18: The plots show the flowing surface layer of the bead mixtures. The data was extracted from the surface coordinate positions and ordered by velocity and ratio of particles. The tracer used for this run was the 5 mm tracer with varying ratios of mixtures. Between plots G-I, the S-shaped profile becomes more prominent indicating that increasing the speed yields a more obvious S-shaped profile.

The graphs above in Figure 18, indicate a relationship between the speed of the tumbling mill with the S-curve profile. As speed increases, the gradient of the profile towards increasing x positions increases. At higher rotational speeds the surface becomes S-shaped thus making it harder to determine the angle of repose, an important ingredient in modelling flow regimes using simulations.

The 5mm beads are substantially smaller and lighter therefore as the speed increases, they

enter a cascading/catarracting motion which can be seen when comparing Figures A-B, D-F and G-I.

The effect of particle size and rotational speed can be determined by comparing the 5 mm and 10 mm tracer used for varying speeds. In Figure 19, the 10 mm tracer was used for the same speed range. This can be compared to the 5mm tracer to determine the effect bead size makes on the S-curved profile i.e. to determine the effect size ratio makes.

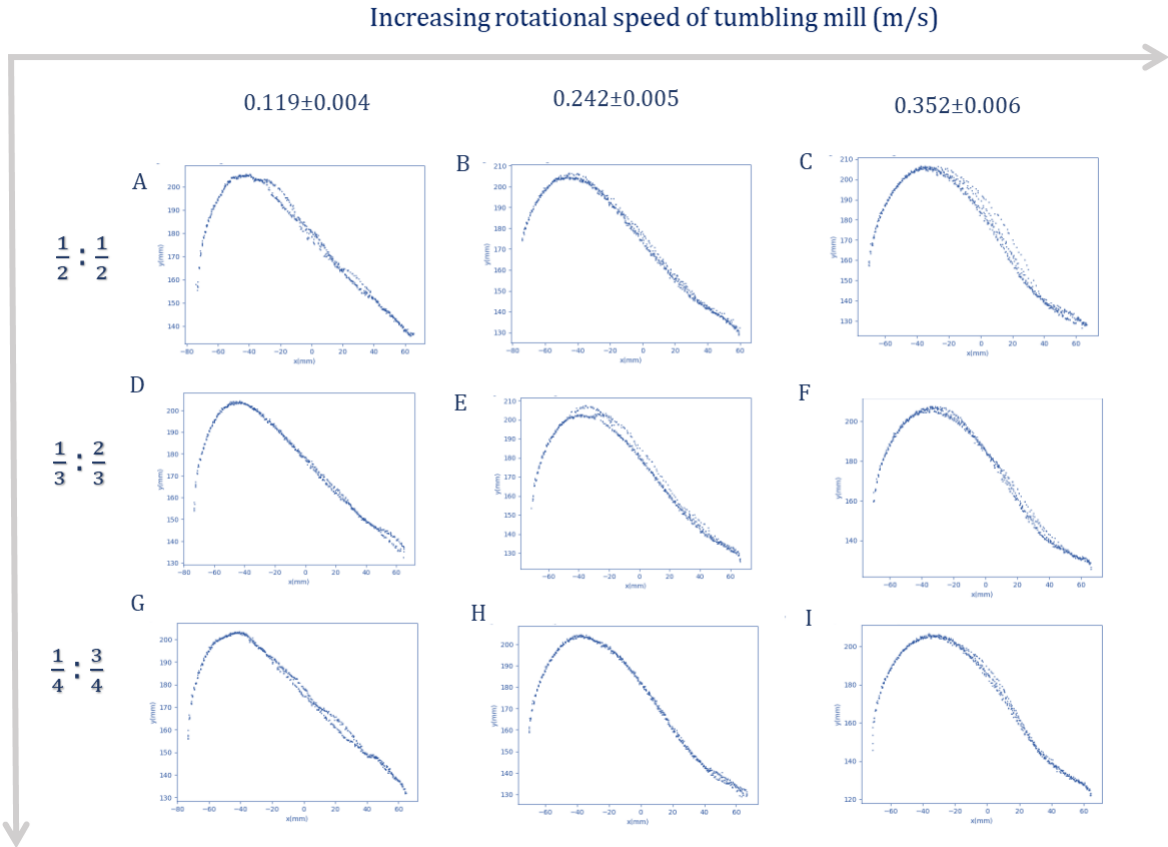


Figure 19: The plots show the flowing surface layer of the bead mixtures. The data was extracted from the surface coordinate positions and ordered by velocity and ratio of particles. The tracer used for this run was the 10 mm tracer with varying ratios of mixtures. In plots C, F and I, the prevalence of the S-shaped curve can be seen in all the plots while in plots A,D and G the layer resembles a linear relation.

By comparing the 5 mm and 10 mm tracer profiles, it can be inferred that with decreasing size ratios, the scaled maximum surface area decreases and the active surface layer becomes more S-shaped. The occurrence of an S-shaped profile at higher rotational speeds could be due to inertial[¶] forces which cannot be determined due to the low speeds used during this investigation.

[¶]Where the inertial force refers to the centripetal force one would obtain at faster speeds - see Section 2.1.2

5.3 Particle velocity plots

Figures 20 and 21 below show the velocity vector fields of the particles in the rotating drum at the various rotation speeds and 5 mm to 10 mm bead ratios. These plots were created using the velocity calculations described in Section 4.3

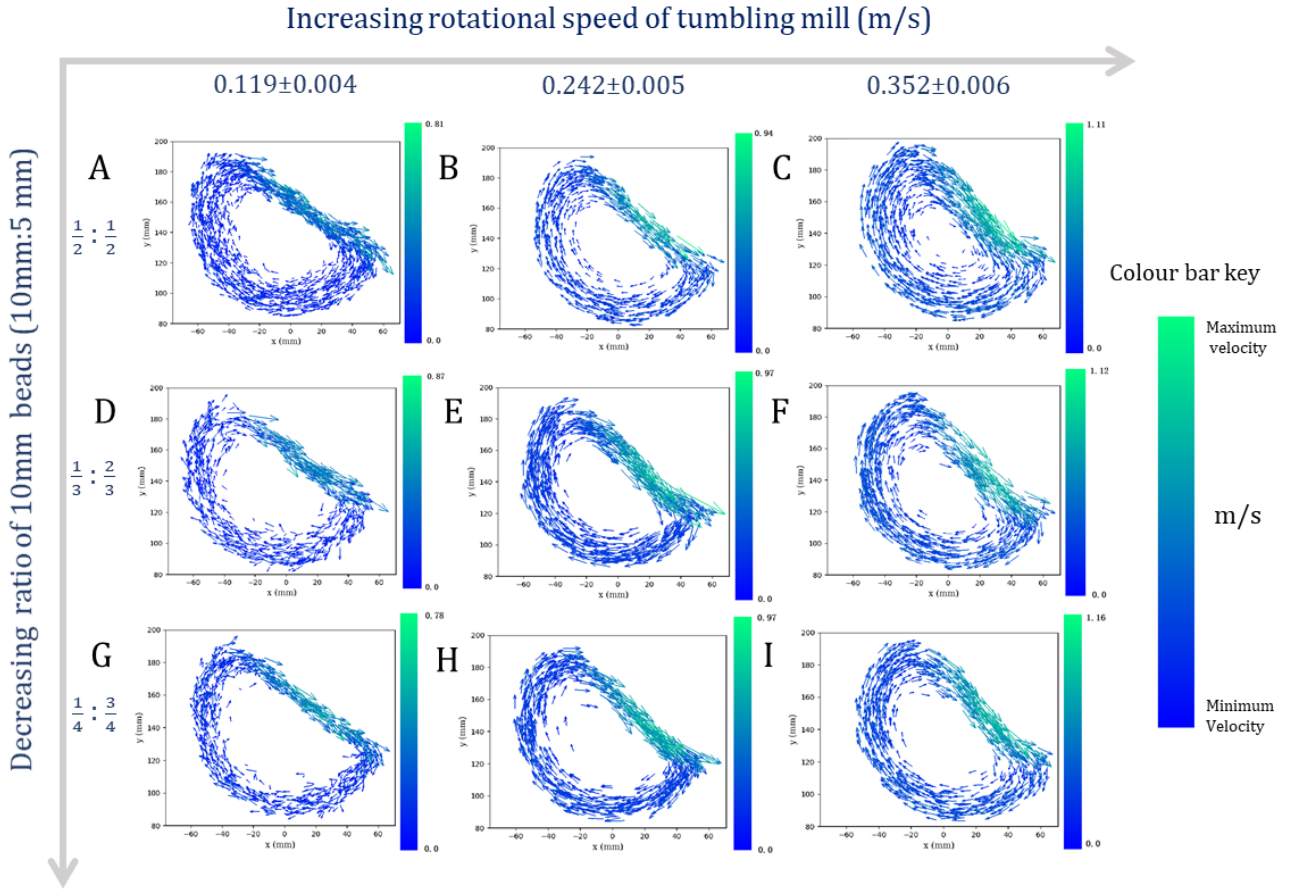


Figure 20: Velocity quiver plots, for all ratio and speed permutations, of the 10 mm glass bead tracer. The colour bars on each plot indicate the maximum and minimum velocity of the particle calculated via the method described in 4.3. The rotational speed of the drum and the mass ratio of 10mm beads is indicated on the top and left side of the figure, respectively.

The plots in figure 20 show that where the 10 mm bead touch the surface of the drum, we find the motion to be almost entirely uniform, with exception of the shoulder of the motion where gravitational effects slow the mass. However, the system is not porous enough to allow a flow downwards and the particles reach the surface and flow down increasing in velocity drastically before reentering at the toe region. This process is followed by the 10mm particle regardless of ratio or drum speed. As would be expected, the maximum velocity reached by the beads increases as the rotational speed of the tumbling mill increases.

The behaviour derived from the velocity fields in figure 20, shows that as seen in the frequency plots (previous section), the 10 mm particles tend to occupy a wider band of area

with increasing speed. This is the case looking at subplots A-C, D-F and G-I. The bands of segregation are less contained indicating a more mixed flow of 5 mm to 10 mm particles in the regions between the centre of circulation and the drum circumference. This phenomena is less prevalent when the ratio of 10 mm particles is decreased, hence it is fair to assume that the outer band is the preferred location of the 10 mm particles.

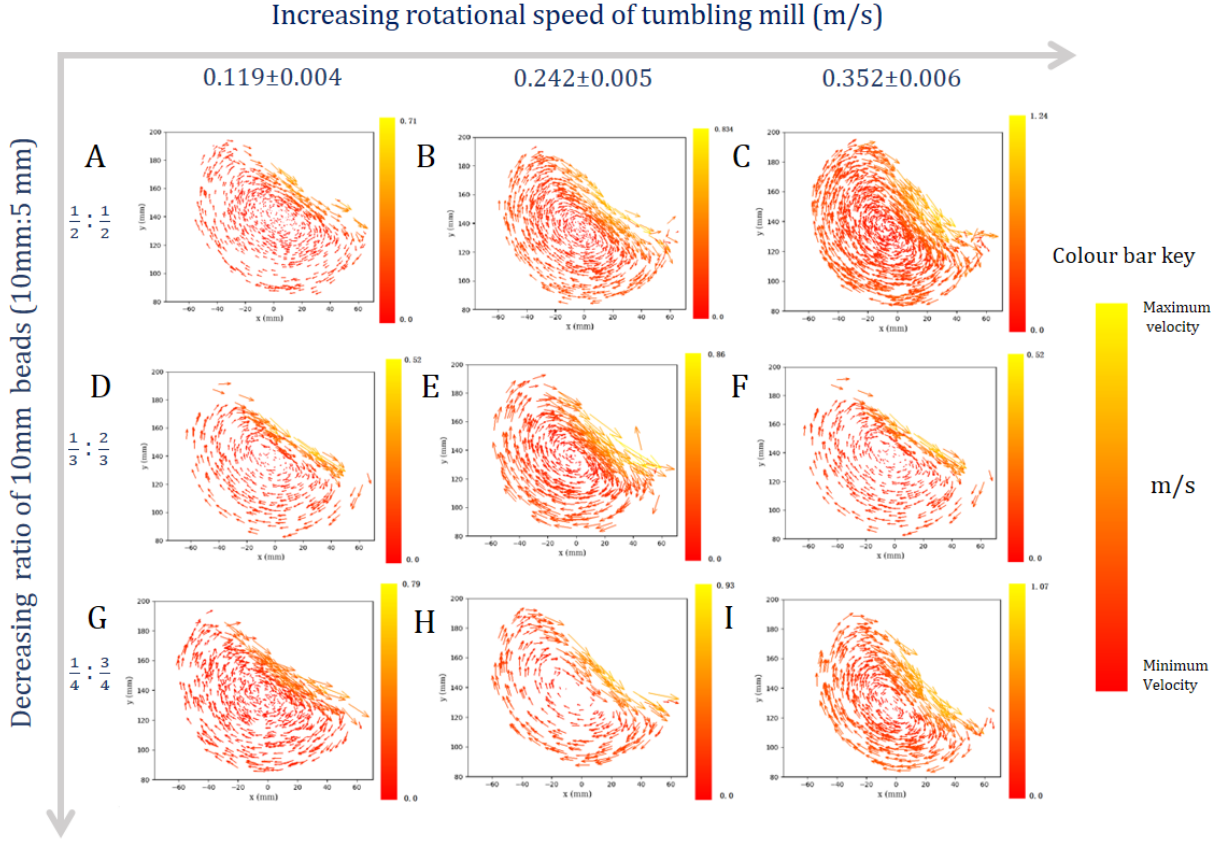


Figure 21: Velocity quiver plots, for all ratio and speed permutations, of the 5 mm glass bead tracer. The colour bars on each plot indicate the maximum and minimum velocity of the particle calculated via the method described in 4.3. The rotational speed of the drum and the mass ratio of 5mm beads is indicated on the top and left side of the figure, respectively.

The velocity plots in figure 21 follow a similar behaviour to that shown in figure 19 for the particles that touch the surface of the drum. However, from these velocity plots and the frequency plots in section 5.2.1 we can see that the 5 mm beads are mainly concentrated near the center of the drum, away from the edges. The particles near the center also undergo almost uniform motion, with the velocities of the particles decreasing with decreasing distance from the center of the drum.

Looking at A, B and C we can see that as we increase the speed, the velocity vectors tend to be more evenly distributed across the whole plot. This pattern is not apparent in all of the plots.

As we can see in Figures 20 and 21, all of the maximum velocity vectors tend to concentrate around the surface of the distribution, with the quantity of maximum velocity vectors on the surface increasing as we increase the rotational speed of the mill. The minimum velocities tend to remain in the centre for all of the plots.

In some of the plots, most prominently in B, C, H and I, we can see that in the toe region on the bulk surface edge some of the velocity vectors from below the surface go past and over the surface. This could be showcasing some cataracting motion of the particles.

5.4 Position Probabilities

In Figure 17, as the speed of the drum and ratio of particle changes; the different bead types are segregated into separate regions based on the volume and mass differences between the 5 mm and 10 mm beads. However, our descriptions of these effects are as of yet largely qualitative. It is useful to find the probability density functions (PDFs) of particles with reference to the radial distance from the Center of Circulation (CoC), showing at which radial distances the bead is most likely to be found in for any given rotation. This will provide us with a way to more accurately and quantitatively describe the segregation effects observed in figure 17.

To calculate the PDFs for each experimental run, position x with respect to time was plotted, with the initial 20 seconds of data removed to account for any initial conditions affecting the measurements. The data followed a mostly sinusoidal pattern. A rough estimate for the CoC was determined by calculating the midpoints of the maximum and minimum x and y values. All radial distances were then calculated using this point as the central location.

With this method the bead would have no probability of being at the CoC, since the minimum x position is almost always going to be outside of the CoC, unless the rotation path of the bead is contained within it. This doesn't mean that the bead didn't pass through the CoC, but just that this would not be reflected with this method.

Following this, a peak finding algorithm [25] was applied to the plotted data to find its turning points at minimum x value, with the data smoothed using a moving average with window size 10 to reduce the number of falsely identified peaks.

At each peak, the radial distance was calculated. These distances were binned into 5 mm bands, counting the number of times the bead fell into one of these bands. 5 mm bands were chosen since this was the minimum bead size in the drum, and therefore a likely distance between bands in different rotations. From this, the PDF is generated which shows the probability of a bead being in a particular band for a single rotation of the drum.

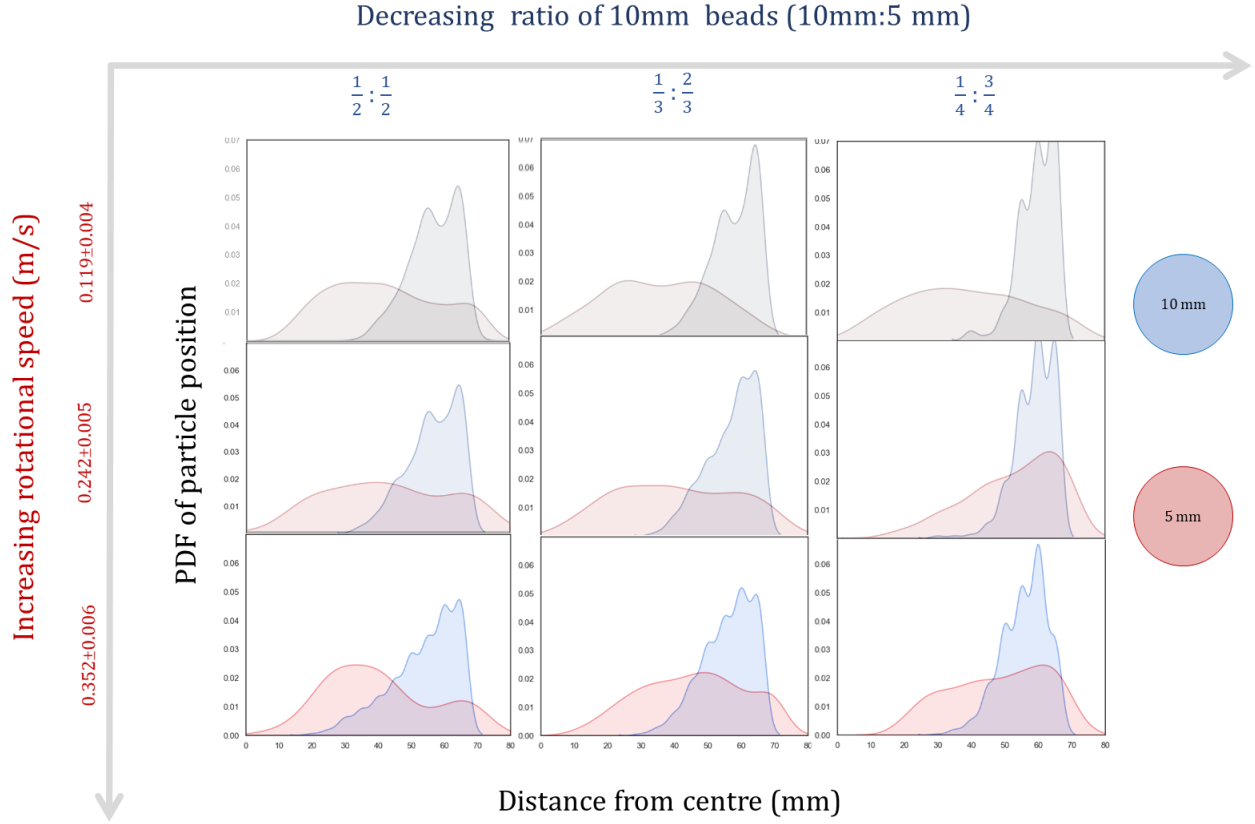


Figure 22: Probability density functions of the 5 mm (red) and 10 mm (blue) at a distance from the Center of Circulation (CoC).

From Figure 22, in all cases the 10 mm beads were more likely to be found at larger distances from the CoC in comparison to the 5 mm beads. This confirms our observations in Figure 17 which showed that the larger beads tended to remain on the outside of the drum, whereas the smaller beads tended to collect in the CoC.

When decreasing the ratio of 10 mm beads we can also see that the distance distribution of the 10 mm beads becomes narrower, with beads being less likely to be found at smaller radial distances. This is expected since the larger beads tend to remain towards the outside of the drum, and since there is a smaller quantity 10 mm beads in the drum the region in which these beads collect becomes smaller, restricting them to a smaller number of bands within the drum.

We would expect the opposite effect with the 5mm beads since a larger quantity of these beads infers that there would be more bands in the drum occupied by the smaller beads. This is indicated by the distance distributions of the 5 mm beads becoming more spread out with increasing quantity occupying a larger radial distance region in the drum.

With increasing speed, we can see that the distance distribution peaks become slightly wider

with the probability of the 5 mm beads being found at larger radial distances increasing (and the different size particle distributions overlapping more). This is likely due to the increased rotational speed of the beads which increased the frequency of the particles entering the free surface (due to the fact that the beads are completing full rotations in the drum at higher frequencies), as well as making the motion of these particles more erratic and unpredictable during a rotation. This leads to more disordered transitions between rotations. This shows that as the speed increases the 5 mm beads are more likely to intersperse with the 10 mm beads rather than the two bead types separating into more distinct regions compared to lower speeds.

5.5 Axial Effects

5.5.1 Energy Fluctuations with Occupancy

According to Fan and Hill [10], particles of all size tend to occupy regions of lower fluctuation energy. Furthermore, smaller particles have an even greater tendency of moving away from regions of high fluctuation energy. In order to see if this phenomenon is taking place, the occupancy plots need to be compared to the fluctuation energy distribution. The colour bar keys below detail refer to the plots that follow.

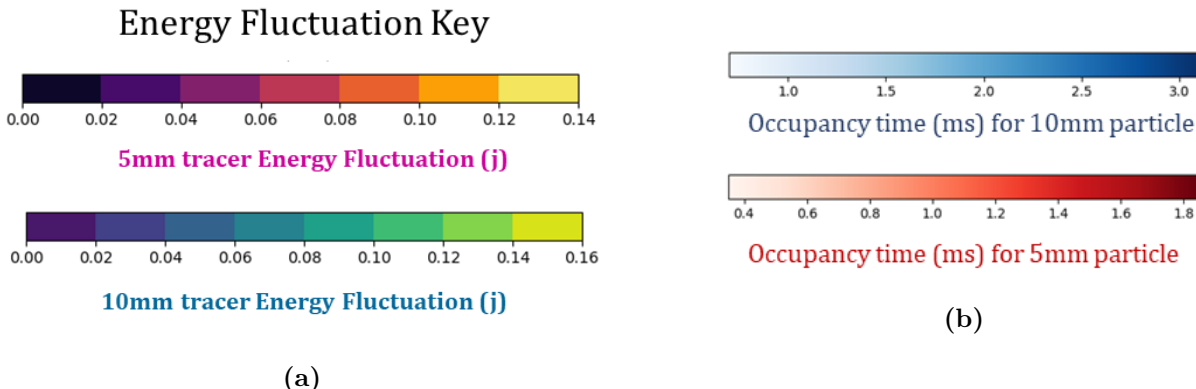


Figure 23: Colour bars relating to the 3 plots to follow. All units are described as above, with (a) relating specifically to the energy fluctuation heat maps and (b) relating to the occupancy time

$$\frac{1}{2} : \frac{1}{2}$$

Increasing rotational speed of tumbling mill (m/s)

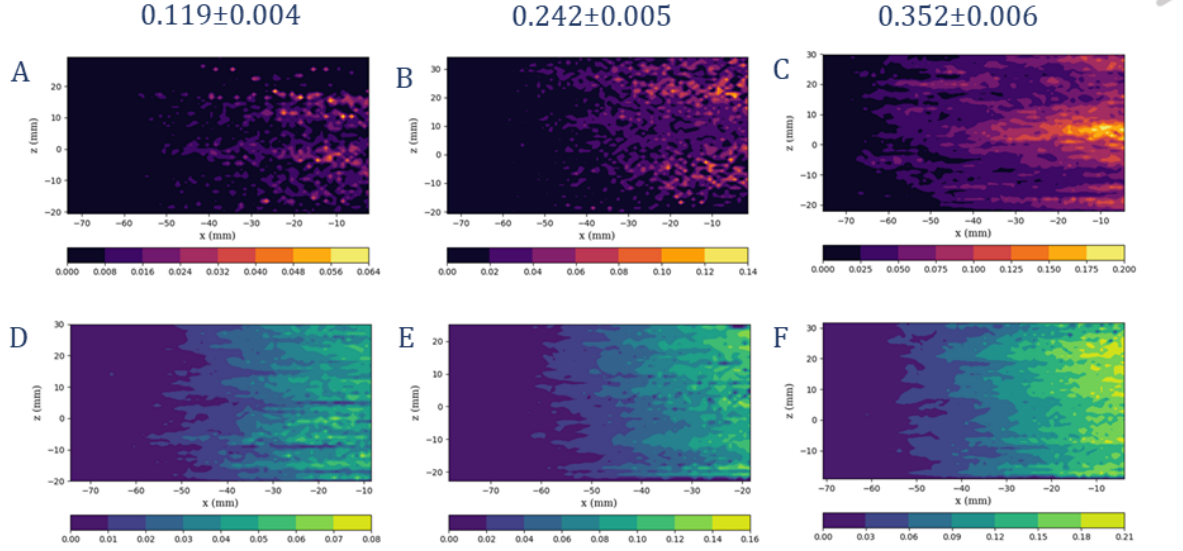


Figure 24: Fluctuation energy heat maps for the $\frac{1}{2} : \frac{1}{2}$ (10 mm : 5 mm) glass bead ratio.

$$\frac{1}{2} : \frac{1}{2}$$

Increasing rotational speed of tumbling mill (m/s)

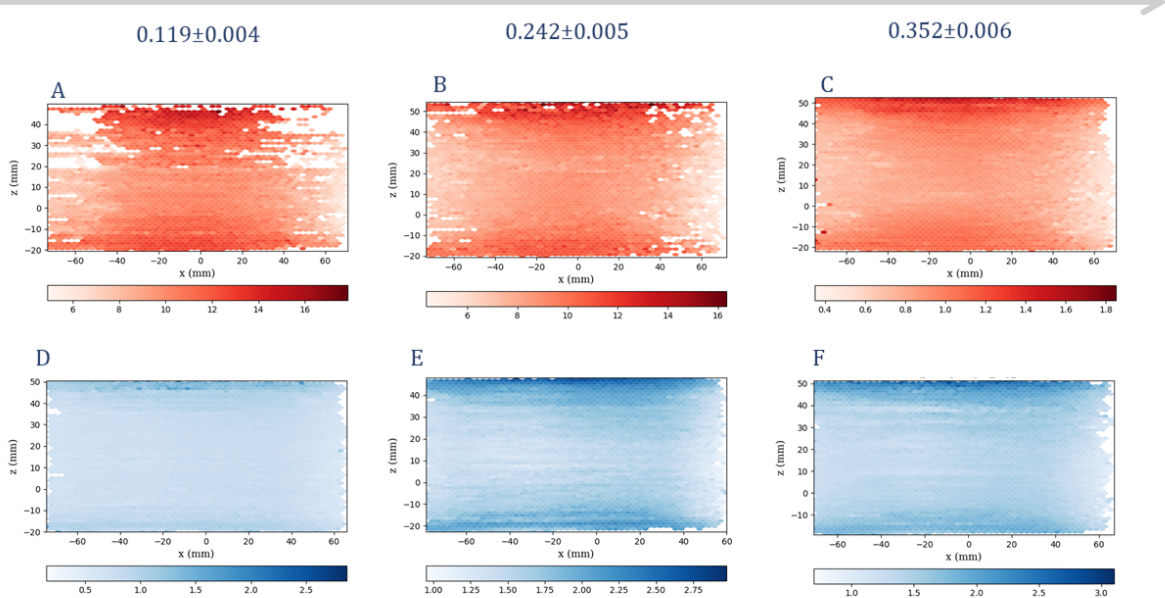


Figure 25: Occupancy time plots for the $\frac{1}{2} : \frac{1}{2}$ (10 mm : 5 mm) glass bead ratio.

$$\frac{1}{3} : \frac{2}{3}$$

Increasing rotational speed of tumbling mill (m/s)

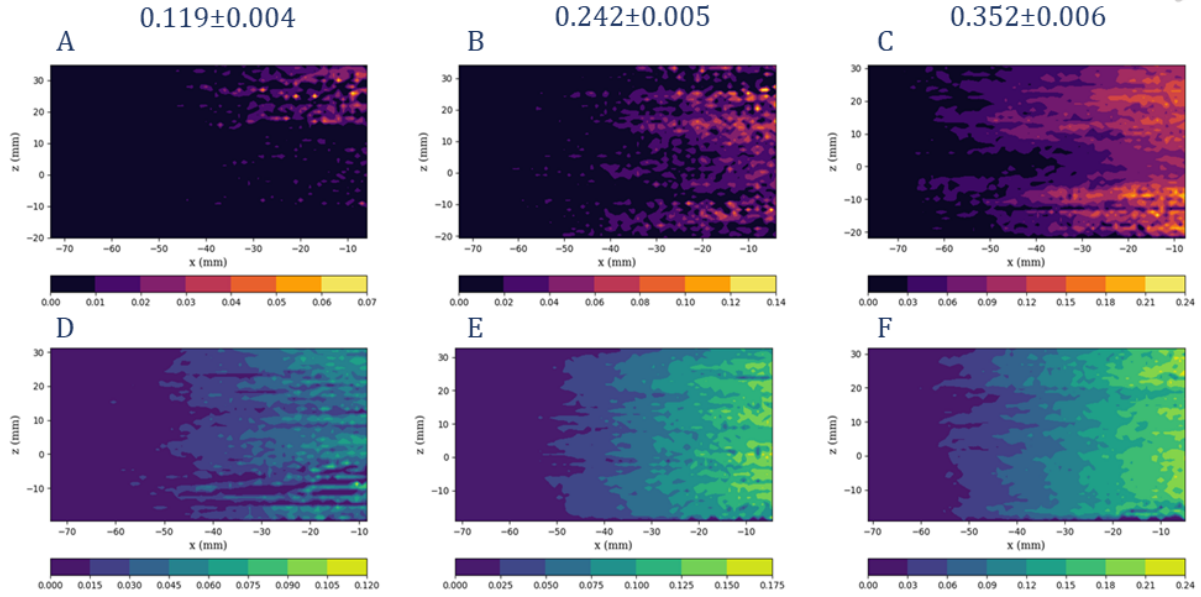


Figure 26: Fluctuation energy heat maps for the $\frac{1}{3} : \frac{2}{3}$ (10 mm : 5 mm) glass bead ratio.

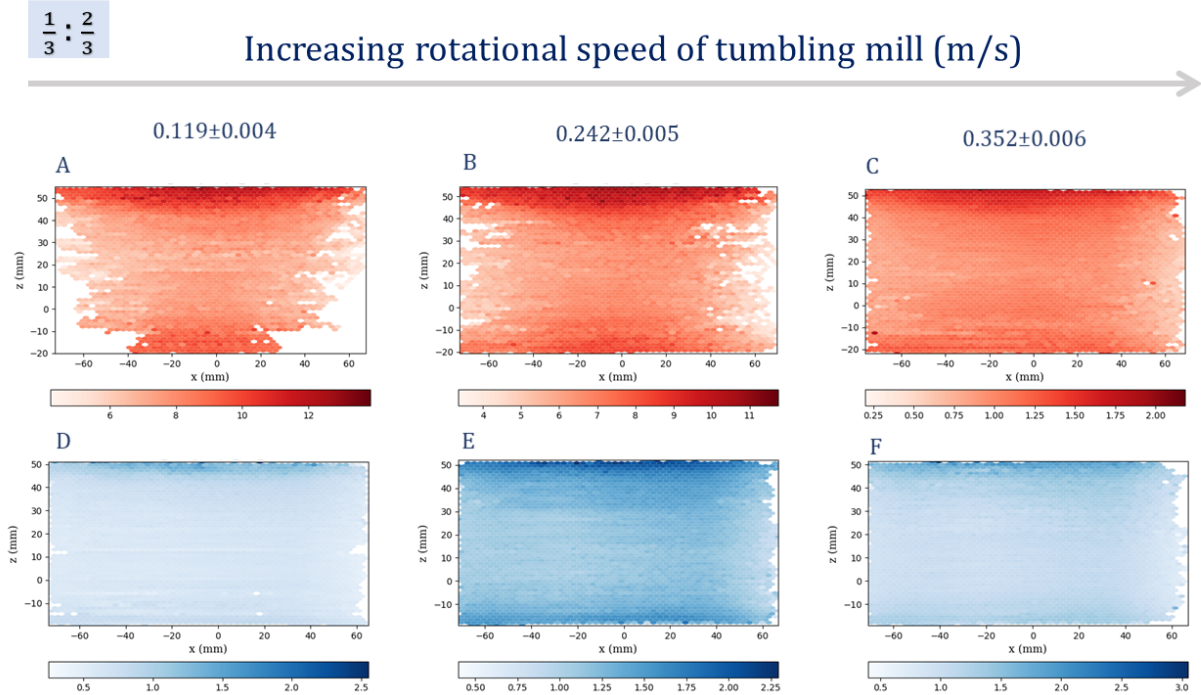


Figure 27: Occupancy time plots for the $\frac{1}{3} : \frac{2}{3}$ (10 mm : 5 mm) glass bead ratio.

$$\frac{1}{4} : \frac{3}{4}$$

Increasing rotational speed of tumbling mill (m/s)

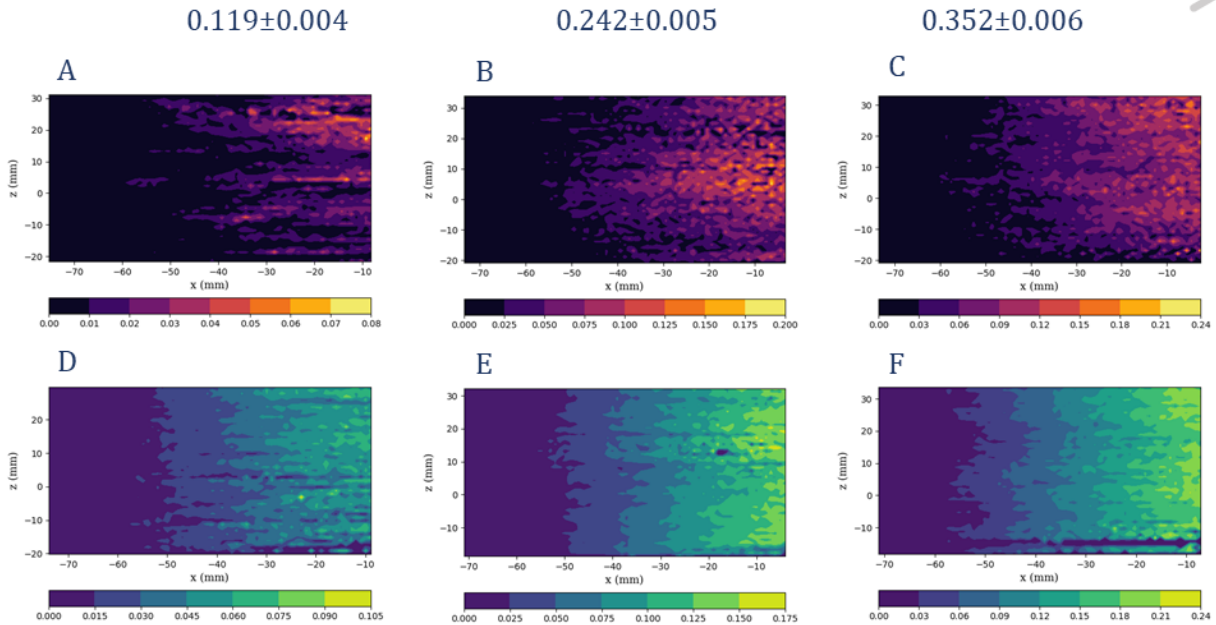


Figure 28: Fluctuation energy heat maps for the $\frac{1}{4} : \frac{3}{4}$ (10 mm : 5 mm) glass bead ratio.

$$\frac{1}{4} : \frac{3}{4}$$

Increasing rotational speed of tumbling mill (m/s)

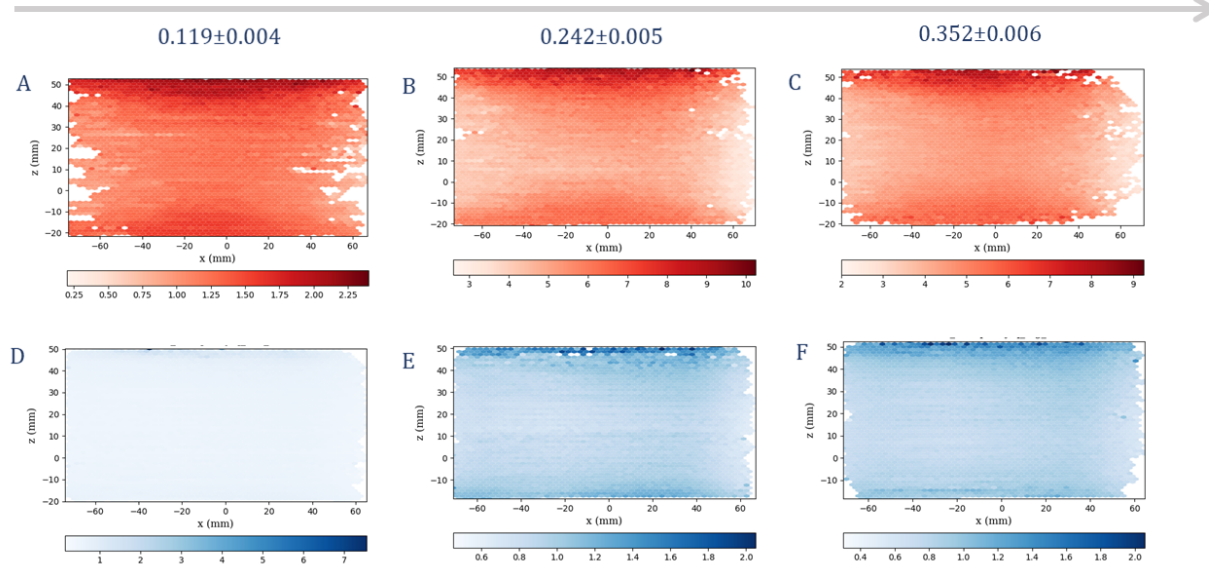


Figure 29: Occupancy time plots for the $\frac{1}{4} : \frac{3}{4}$ (10 mm : 5 mm) glass bead ratio.

In general “Streaks” of low fluctuation energy extending in the x-direction are visible in all fluctuation energy plots. When comparing these ‘streaks’ to the occupancy plots one can see that in most cases the streaks correspond to a higher occupancy time. In figures 25 (F,E) and 24 (F,E) this feature is particularly profound. Comparing the 5 mm and 10 mm particles: the horizontal streaks of low fluctuation energy are less pronounced for the 10 mm particle. In the occupancy plots (ignoring the boundaries), horizontal streaks of darker colours are visible, indicative of larger occupancy times. These regions where particles spent more time appear to overlap with regions of low fluctuation energy. This is in agreement with the theory that predicts that all types of particles tend to move towards regions of low fluctuation energy. Looking at plots A, B and C in Figures 25 and 24 we see that the bulk toe region (right hand side of plots) exhibits higher fluctuation energies increasing with rotational speed.

6 Discussion and Conclusions

The analysis detailed in the previous section all indicated that the segregation of the particles is maintained until such a speed that ceteracting motion was present in the particle motion. The S-curve of the 10mm beads remains unaffected by the ratio of 5mm particles. Furthermore, in any ratio it is very likely that a 10mm particle will be found on the outskirts of the drum. The 5mm particles at the highest speed used, enter sometimes enter ‘free flight’ but this free flight is more likely with a larger ratio of 10mm beads. This perhaps indicates that the 5mm beads at the shoulder of the motion roll over the 10mm beads and find it difficult to reenter the toe region. This is further predicted when observing the fluctuation energy heat map figure 24(C) where the fluctuation energy is extreme in the toe region.

It seems that the particles in the xz plane seem to group together in rings. Looking at figures 24, 27 and 29 we can see that the energy fluctuations have horizontal streaks of uniform energy fluctuation change, but do not actually have a z dependence. This phenomena occurs in all data sets, showing that the axial segregation of particles does take place.

6.1 Further Work

One of the largest issues with positional data was the slight displacement of the drum after each measurement. This was due to the drum needing to be shaken or beads needing to be replaced. To avoid this further work should be conducted with a calibration points taken before each run. This will ensure all data can be accurately aligned. Analysis could also be improved via retaking the data with the lower activity tracer. For indication of the data sets of interest please

6.1.1 Mayavi Python Vector analysis

For the velocity plotting a python package called *Mayavi* [26] was used. This provides internal binning and fast compilation of large data sets. In this research could be improved greatly by using more of it's features. Specifically, When combining velocity data from the 5mm and 10mm the following is produced. Mayavi has a feature where vector fields can be sliced into planes. This could be valuable for future axial segregation analysis. Data can be analysed three dimentionally without memory issues.

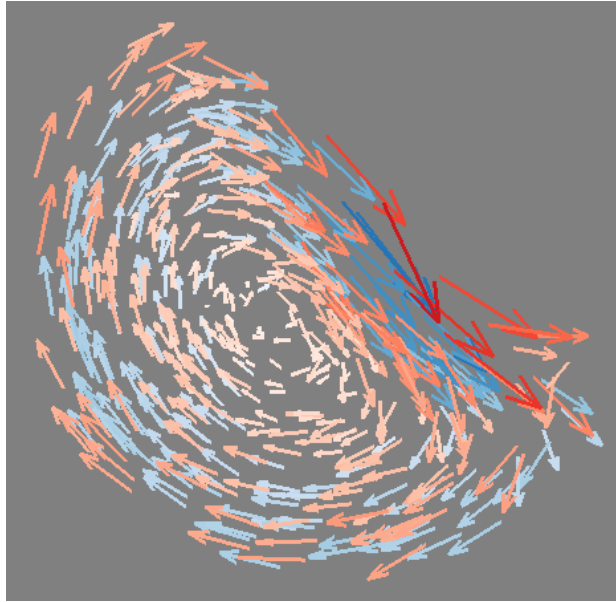


Figure 30: Two radial velocity vector plots for the $\frac{1}{2} : \frac{1}{2}$ 10mm:5mm bead ratio at 0.352 ± 0.006 m/s rotational velocity.

References

- [1] C. R. K. Windows-Yule, B. J. Scheper, A. J. van der Horn, N. Hainsworth, J. Saunders, D. J. Parker, and A. R. Thornton, “Understanding and exploiting competing segregation mechanisms in horizontally rotated granular media,” *New Journal of Physics*, vol. 18, p. 023013, jan 2016.
- [2] A. Buffler, K. Cole, T. Leadbeater, and M. van Heerden, “Positron emission particle tracking: A powerful technique for flow studies,” *International Journal of Modern Physics: Conference Series*, vol. 48, p. 1860113, 01 2018.
- [3] T. W. Leadbeater, D. J. Parker, and J. Gargiuli, “Positron imaging systems for studying particulate, granular and multiphase flows,” *Particuology*, vol. 10, no. 2, pp. 146 – 153, 2012. Advances in Characterization and Modeling of Particulate Processes.
- [4] A. Morrison, I. Govender, A. Mainza, and D. Parker, “The shape and behaviour of a granular bed in a rotating drum using eulerian flow fields obtained from pept,” *Chemical Engineering Science*, vol. 152, pp. 186 – 198, 2016.
- [5] J. M. Ottino and D. V. Khakhar, “Mixing and segregation of granular materials,” *Annual Review of Fluid Mechanics*, vol. 32, no. 1, pp. 55–91, 2000.
- [6] J. Mellmann, “The transverse motion of solids in rotating cylinders—forms of motion and transition behaviour,” *Powder Technology*, vol. 118, pp. 251–270, 08 2001.
- [7] D. de Klerk, I. Govender, and A. Mainza, “Geometric features of tumbling mill flows: A positron emission particle tracking investigation,” *Chemical Engineering Science*, vol. 206, pp. 41 – 49, 2019.
- [8] G. Juarez, P. Chen, and R. M. Lueptow, “Transition to centrifuging granular flow in rotating tumblers: a modified froude number,” *New Journal of Physics*, vol. 13, p. 053055, May 2011.
- [9] A. V. Orpe and D. V. Khakhar, “Scaling relations for granular flow in quasi-two-dimensional rotating cylinders,” *Physical Review E*, vol. 64, no. 3, pp. 1 – 13, 2001.
- [10] Y. Fan and K. M. Hill, “Theory for shear-induced segregation of dense granular mixtures,” *New Journal of Physics*, vol. 13, p. 095009, sep 2011.
- [11] Centre for Minerals Research, *Computational Modelling*, 2019.
- [12] K. Tanaka, M. Nishida, T. Kunimochi, and T. Takagi, “Numerical and experimental studies for the impact of projectiles on granular materials,” in *Handbook of Conveying and Handling of Particulate Solids* (A. Levy and H. Kalman, eds.), vol. 10 of *Handbook of Powder Technology*, pp. 263 – 270, Elsevier Science B.V., 2001.
- [13] H. H. Hu, “Chapter 10 - computational fluid dynamics,” in *Fluid Mechanics (Fifth Edition)* (P. K. Kundu, I. M. Cohen, and D. R. Dowling, eds.), pp. 421 – 472, Boston: Academic Press, fifth edition ed., 2012.

- [14] K. W. Linfield and R. G. Mudry, *Pros and Cons of CFD and Physical Flow Modeling*. Airflow Sciences Corporation, 2008.
- [15] T. Leadbeater, *Positron Emission Particle Tracking*.
- [16] P. Ornella, *Glass beads as grinding media*.
- [17] E. Mccutchan, “Nuclear data sheets for $a = 68$,” *Nuclear Data Sheets*, vol. 113, no. 6-7, p. 1735–1870, 2012.
- [18] M.-M. Bé, V. Chisté, C. Dulieu, M. Kellett, X. Mougeot, A. Arinc, V. Chechev, N. Kuzmenko, T. Kibédi, A. Luca, and A. Nichols, *Table of Radionuclides*, vol. 8 of *Monographie BIPM-5*. Pavillon de Breteuil, F-92310 Sèvres, France: Bureau International des Poids et Mesures, 2016.
- [19] X. Fan, D. J. Parker, and M. D. Smith, “Labelling a single particle for positron emission particle tracking using direct activation and ion-exchange techniques,” *Nucl. Instruments Methods Phys. Res. Sect. A Accel. Spectrometers, Detect. Assoc. Equip.*, vol. 562, p. 345–350, Jun 2006.
- [20] K. Cole, A. Buffler, J. J. Cilliers, I. Govender, J. Y. Heng, C. Liu, D. J. Parker, U. V. Shah, M. van Heerden, X. Fan, and et al., “A surface coating method to modify tracers for positron emission particle tracking (pept) measurements of froth flotation,” *Powder Technology*, vol. 263, p. 26–30, 2014.
- [21] M. van Heerden, “The purification of ^{68}ga from an aged $^{68}\text{ge}/^{68}\text{ga}$ generator and the labelling of the product and ^{18}f in ion exchange for pept studies 2010,”
- [22] M. van Heerden, “The performance analysis of ag mp-1 anion exchange resin $^{68}\text{ge}/^{68}\text{ga}$ generators and the radiolabelling of ion exchange resins for pept studies 2012,”
- [23] G. F. Knoll, *Radiation Detection and Measurement*. Wiley, 4th ed., 2010.
- [24] C. Boyd, *Radiation Protection Standard*. iThemba Labs, 2006.
- [25] S. Wheaton, *More Advanced Model Fitting and Plotting*. University of Cape Town, 2017.
- [26] P. Ramachandran and G. Varoquaux, “Mayavi: 3D Visualization of Scientific Data,” *Computing in Science and Engineering*, vol. 13, no. 2, pp. 40–51, 2011.
- [27] A. Buffler, *Introduction to Measurement in the Physics Laboratory: A Probabilistic Approach*, 2016.

A Uncertainty Budget

Measurand	Device	Value	Evaluation	PDF
Mass of bead	Digital scale	1.238 ± 0.001 kg	B	Rectangular
Height of supporting table	Metre rule	73.5 ± 0.05 cm	B	Triangular
Depth of central axis	Measuring tape	11.75 ± 0.05 cm	B	Triangular
Inner radius of drum	Measuring tape	14.5 ± 0.05 cm	B	Triangular
Depth of drum	Measuring tape	7.5 ± 0.05 cm	B	Triangular
Velocity of motor rollers	Digital scale	2.99 ± 0.01 rev/s	B	Rectangular
Velocity of motor rollers	Digital scale	2.04 ± 0.01 rev/s	B	Rectangular
Velocity of motor rollers	Digital scale	1.00 ± 0.01 rev/s	B	Rectangular
Activity of tracer	Ionisation chamber	956 ± 1 μ Ci	A	Rectangular
Activity of tracer	Ionisation chamber	117 ± 1 μ Ci	A	Rectangular
Activity of tracer	Ionisation chamber	533 ± 1 μ Ci	A	Rectangular
Elapsed time	Digital stopwatch	10.000 ± 0.001 min	B	Rectangular
Position of tracer	PEPT	Various	A	Normal

Table 7: Table showing the uncertainty budget of the measurements in the experiment all listed with the device was used for measurement, the type of evaluation and the Probability Density Function (PDF) used to evaluate bounds of uncertainty [27].